

ISO Mid-Infrared Spectra of Reflection Nebulae¹

K. I. Uchida^{2,3,4}, K. Sellgren², M. W. Werner⁵, and M. L. Houdashelt^{2,6}

Accepted for publication in the *Astrophysical Journal*, 5 October 1999

ABSTRACT

We present 5 – 15 μm imaging spectroscopy of the reflection nebulae vdB 17 (NGC 1333), vdB 59 (NGC 2068), vdB 101, vdB 111, vdB 133 and vdB 135, obtained with the infrared camera and circular variable filter wheel on the *Infrared Space Observatory (ISO)*. These nebulae are illuminated by stars with $T_{\text{eff}} = 3,600 \text{ K} - 19,000 \text{ K}$, implying ultraviolet (UV; $\lambda < 400 \text{ nm}$) to total stellar flux ratios of $F_{(\lambda < 400 \text{ nm})}/F_{\text{total}} = 0.01 - 0.87$. We detect the infrared emission features (IEFs) at 6.2, 7.7, 8.6, 11.3, and 12.7 μm , broad emission features at 6 – 9 μm and 11 – 13 μm , and 5 – 15 μm continuum emission, from the interstellar medium in vdB 17, vdB 59, and vdB 133 ($F_{(\lambda < 400 \text{ nm})}/F_{\text{total}} = 0.22 - 0.87$), and place upper limits on the emission from the interstellar medium in vdB 101, vdB 111, and vdB 135 ($F_{(\lambda < 400 \text{ nm})}/F_{\text{total}} = 0.01 - 0.20$).

Our goal is to test predictions of models attributing the IEFs to polycyclic aromatic hydrocarbons (PAHs). Interstellar models predict PAHs change from singly ionized to neutral as the UV intensity, G_0 , decreases. The ratio of PAH emission at 6 – 10 μm to PAH emission at 10 – 14 μm is expected to be ten times higher in ionized than neutral PAHs.

We observe no spectroscopic differences with varying T_{eff} . We analyze the spectra of vdB 17 and vdB 59 as a function of distance from the star, to see how

¹Based on observations with ISO, an ESA project with instruments funded by ESA Member States (especially the PI countries: France, Germany, the Netherlands and the United Kingdom) and with the participation of ISAS and NASA.

²Dept. of Astronomy, The Ohio State University, 140 West 18th Ave., Columbus, OH 43210-1173

³kuchida@astrosun.tn.cornell.edu

⁴Current Address: Cornell University, 108 Space Sciences Bldg, Ithaca, NY 14853

⁵Jet Propulsion Laboratory, MS 264-767, 4800 Oak Grove Dr., Pasadena, CA 91109

⁶Current Address: Dept. of Physics & Astronomy, Johns Hopkins University, 3400 N. Charles St., Baltimore, MD 21218

the spectra depend on G_0 within each source. The only quantitative difference we find is a *broadening* of the $7.7 \mu\text{m}$ IEF at $G_0 = 20 - 60$ within vdB 17. We observe only a 40% change in the $6 - 10 \mu\text{m}$ to $10 - 14 \mu\text{m}$ flux ratio over $G_0 = 20$ to 6×10^4 .

Subject headings: reflection nebulae — dust, extinction — ISM: lines and bands — infrared: ISM: lines and bands — infrared: ISM: continuum

1. Introduction

The infrared emission features (IEFs) at 3.3 , 6.2 , 7.7 , 8.6 , 11.3 and $12.7 \mu\text{m}$, and their associated continuum, have been the subject of intense study over the last decade. The IEF strengths correlate with the C/O ratio in planetary nebulae, suggesting a carbon-based carrier (Roche & Aitken 1986; Cohen et al. 1986, 1989). Duley & Williams (1981) were the first to comment that some IEF wavelengths are characteristic of the bending and stretching modes of various C–H and C–C bonds in aromatic hydrocarbons. There has since been a steady accumulation of evidence, both laboratory and observational, in support of this assertion. The specific nature of the carrier(s), however, is yet to be determined. The IEFs have been attributed to polycyclic aromatic hydrocarbon (PAH) molecules (Léger & Puget 1984; Allamandola, Tielens, & Barker 1985) and to more amorphous materials containing aromatic hydrocarbons (Sakata et al. 1984, 1987; Borghesi, Bussoletti, & Colangeli 1987; Blanco, Bussoletti, & Colangeli 1988; Duley 1988; Papoular et al. 1989). Allamandola, Tielens, & Barker (1989) and Bregman et al. (1989) attribute the broad spectral structures at $6 - 9 \mu\text{m}$ and $11 - 13 \mu\text{m}$, which accompany the IEFs, to PAH clusters and amorphous carbon grains.

The origin of the $1 - 25 \mu\text{m}$ continuum emission, like that of the associated IEF emission, is still the subject of debate. The continuum is observed in regions of very low radiation density, such as reflection nebulae and infrared cirrus, where the grain equilibrium temperature is too low to explain the emission as being thermal in nature (Sellgren 1984; Draine & Anderson 1985; Guillois et al. 1996). It has been attributed to single ultraviolet (UV) photon excitation of very small grains (Sellgren, Werner, & Dinerstein 1983; Sellgren 1984), to PAH molecular fluorescence (Léger & Puget 1984; Allamandola et al. 1985, 1989; Puget & Léger 1989), and to hydrogenated amorphous carbon grain luminescence (Duley & Williams 1988; Duley 1988).

The IEF carriers are a ubiquitous component of the interstellar medium (ISM). Past studies have found IEFs in *emission* near Galactic H II regions, reflection nebulae, planetary

nebulae, proto-planetary nebulae, and the diffuse ISM of our own and other galaxies (see reviews by Aitken 1981; Allamandola et al. 1989; Puget & Léger 1989; Geballe 1997; and Tokunaga 1997). The $6.2 \mu\text{m}$ IEF has recently been detected in *absorption* in the diffuse ISM (Schutte et al. 1996, 1998). The $3.3 \mu\text{m}$ IEF may have also been detected in *absorption* in molecular clouds (Sellgren, Smith, & Brooke 1994; Sellgren et al. 1995; Brooke, Sellgren, & Smith 1996; Brooke, Sellgren & Geballe 1999).

IEF spectra have been recently classified into several groups (Geballe 1997; Tokunaga 1997). Class A spectra at $5 - 15 \mu\text{m}$ display narrow IEFs at $6.2, 7.7, 8.6, 11.3$ and $12.7 \mu\text{m}$, as well as associated continuum emission. The $7.7 \mu\text{m}$ IEF is invariably the strongest of the Class A narrow IEFs (Geballe 1997). By contrast, Class B spectra lack the $8.6 \mu\text{m}$ IEF and have notably broader features at 8 and $11.5 \mu\text{m}$ (Kwok, Volk, & Hrivnak 1989). Class B spectra sometimes also show a strong broad emission feature at $8.8 \mu\text{m}$ (Buss et al. 1993). The overwhelming majority of IEF spectra currently measured fall under the category of Class A. Sources with Class A IEFs are typically UV-rich sources, such as the diffuse ISM, reflection nebulae, H II regions, young stars, planetary nebulae and galaxies hosting star formation. By contrast, the half-dozen or so Class B spectra found to date arise from F and G-type post-AGB stars forming planetary nebulae (i.e. proto-planetary nebulae; Geballe et al. 1992).

Well-developed theoretical work exists for the absorption and emission properties of PAHs, inspired by the hypothesis that PAHs are responsible for the IEFs. Mixtures of PAHs and other dust components have been used to model the UV and visible extinction curve and the infrared emission observed in the ISM (Puget, Léger, & Boulanger 1985; Chlewicki & Laureijs 1988; Désert, Boulanger & Puget 1990; Joblin, Léger, & Martin 1992; Siebenmorgen & Krügel 1992; Schutte, Tielens, & Allamandola 1993; Dwek et al. 1997; Li & Greenberg 1997; Silva et al. 1998). All of these models include a size distribution of PAHs. Most of these size distributions include large PAHs, expected in the ISM but not yet measured in the laboratory, by extrapolation from laboratory data on smaller PAHs. Interstellar PAHs are predicted to be mainly positively charged and neutral in strong UV fields, and mainly neutral and negatively charged when the UV field is weak (Bakes & Tielens 1994, 1998; Salama et al. 1996; Dartois and d’Hendecourt 1997). Some interstellar models (particularly Désert et al. 1990) include both neutral and ionized PAHs.

These models for the absorption and emission from a size distribution of neutral and ionized PAHs predict that the fraction of the total interstellar extinction curve due to PAH absorption is much larger at UV wavelengths than at visible wavelengths. This is vividly illustrated in Figures 2 and 3 of Désert et al. (1990), Figures 1, 2, and 3 of Joblin et al. (1992), Figures 1*b*, 2*b* and 4*b* of Siebenmorgen & Krügel (1992), Figure 4 of Dwek et al.

(1997), and Figure 3 of Silva et al. (1998). If PAHs contribute more to the total interstellar extinction at UV than visible wavelengths, then PAHs should absorb and re-emit a larger fraction of the total absorption and re-emission by dust in UV-rich sources than in UV-poor sources.

Reflection nebulae are valuable tools for the study of the Class A interstellar IEFs. The localized heating of an interstellar cloud by a nearby, optically visible, star allows us to study the IEFs over varying excitation conditions by observing reflection nebulae illuminated by stars of different effective temperature, T_{eff} . This localized heating also results in brighter infrared emission than would be observed in a similar cloud heated only by the diffuse interstellar radiation field.

Sellgren, Luan, & Werner (1990) analyzed *IRAS* observations of reflection nebulae illuminated by stars with $T_{\text{eff}} = 3,000 \text{ K} - 33,000 \text{ K}$. They observed that the ratio of nebular emission within the *IRAS* 12 μm broadband filter, $\Delta\nu I_\nu(12 \mu\text{m})$, to the total bolometric far-infrared nebular emission, $I_{\text{bol}}(\text{FIR})$, was independent of T_{eff} , for $T_{\text{eff}} = 5,000 \text{ K} - 33,000 \text{ K}$. The total infrared emission of a reflection nebula is due to starlight absorbed and re-radiated by the mixture of molecules and grains responsible for the total interstellar extinction curve. Their observation that $\Delta\nu I_\nu(12 \mu\text{m})/I_{\text{bol}}(\text{FIR})$ is constant over a wide range of T_{eff} implies that the material emitting in the *IRAS* 12 μm band has an absorption curve with a wavelength dependence similar to that of the total interstellar absorption curve over both UV and visible wavelengths.

The Sellgren et al. (1990) observations, finding $\Delta\nu I_\nu(12 \mu\text{m})/I_{\text{bol}}(\text{FIR})$ to be independent of T_{eff} , appear to be in conflict with theoretical predictions that the *IRAS* 12 μm band is dominated by PAH emission and that PAHs contribute more to the total interstellar extinction curve at UV than visible wavelengths (Désert et al. 1990; Joblin et al. 1992; Siebenmorgen & Krügel 1992; Schutte et al. 1993; Dwek et al. 1997; Li & Greenberg 1997; Silva et al. 1998). This is particularly puzzling as both Désert et al. (1990) and Siebenmorgen & Krügel (1992) explicitly fit a mixture of PAHs and other dust components to the observed extinction curves and infrared emission of two reflection nebulae observed by Sellgren et al. (1990): NGC 2023 (vdB 52; $T_{\text{eff}} = 22,000 \text{ K}$) and NGC 7023 (vdB 139; $T_{\text{eff}} = 17,000 \text{ K}$).

The Sellgren et al. (1990) observations could be reconciled with theoretical predictions if other ISM components besides PAHs contribute to the *IRAS* 12 μm broad-band emission in reflection nebulae illuminated by cool stars. Infrared spectroscopy can test whether the fractional contribution of PAHs to the *IRAS* 12 μm broad-band emission of reflection nebulae depends on T_{eff} . Sellgren, Werner, & Allamandola (1996) have searched for spectral differences in the near-infrared emission of reflection nebulae with $T_{\text{eff}} = 3,600 \text{ K} - 33,000 \text{ K}$.

They find that the equivalent width of the $3.3 \mu\text{m}$ IEF in reflection nebulae is independent of T_{eff} , over $T_{\text{eff}} = 11,000 \text{ K} - 22,000 \text{ K}$, but they did not have the sensitivity to detect reflection nebulae illuminated by cooler stars.

This paper presents a spectroscopic imaging study to search for and detail interstellar IEF emission toward a sample of reflection nebulae illuminated by stars with $T_{\text{eff}} = 3,600 \text{ K} - 19,000 \text{ K}$ (Table 1). We obtained our observations with the *Infrared Space Observatory* (*ISO*) camera, ISOCAM (Kessler et al. 1996; C. Cesarsky et al. 1996), using the circular variable filter (CVF). We have reported our initial result, the detection of IEFs toward the UV-poor nebula vdB 133 (illuminated by two stars with $T_{\text{eff}} = 6,800 \text{ K}$ and $12,000 \text{ K}$), in Uchida, Sellgren, & Werner (1998; hereafter Paper I). The goal of our study is to determine whether there are quantitative differences between the excitation of the different IEFs and the continuum emission among nebulae with widely varying T_{eff} . We selected reflection nebulae with previous *IRAS* detections of extended $12 \mu\text{m}$ emission (Sellgren et al. 1990). The unprecedented sensitivity of the cryogenically cooled *ISO* satellite to low surface brightness mid-infrared emission has allowed us to search for IEFs toward the reflection nebulae illuminated by stars later than B-type, where the IEFs are too faint for detection with ground-based or airborne telescopes at ambient temperature.

2. Observations

2.1. Position-Switched Data

We obtained ISOCAM multi-wavelength images of vdB 101, vdB 111, vdB 133 and vdB 135 between 1996 March 19 and 1998 February 16. We used a set of 9 – 10 CVF wavelengths and 1 – 2 narrowband filters toward each nebula, in four sequences. Each sequence contains observations at three to four wavelengths, as listed in Table 2. We observed all four sequences for each nebula, except for vdB 135, where no Sequence 3 observations were made. While the filter observations within a given sequence were performed consecutively in time, the scheduling of the sequences themselves were not necessarily constrained so. Some sequences thus share common wavelength observations to provide a check for consistency with time. All observations were made with a $6''$ pixel⁻¹ scale giving a total field of view of $3'2$ with the 32×32 pixel array. The CVF spectral resolution was $R = \lambda/\Delta\lambda = 40$ and the narrowband filters at $4.5 \mu\text{m}$ (LW1) and $15 \mu\text{m}$ (LW9) had bandpasses of $\Delta\lambda = 1 \mu\text{m}$ and $2 \mu\text{m}$, respectively (ISOCAM Team 1994).

The observations were position-switched (in a 2-cycle sky \rightarrow source \rightarrow sky \rightarrow source sequence), with equal times on the source and sky to allow for the removal of the background

and dark current contributions. The source observations were centered on the illuminating star(s) of each nebula and the sky positions were toward nearby regions deemed free, based on inspection of the *IRAS* 12 μm skyview images, of any significant emission above the Zodiacal component and the local cirrus background. Table 3 lists the positions we observed. The basic integration time per exposure varied between 0.28 s and 10 s, depending on the wavelength and brightness of the central star. The total number of exposures was set to attain a total on-source integration time per filter of ~ 200 s for all observations.

2.2. Full CVF Wavelength Scans

Spectral images of vdB 17 (NGC 1333), vdB 59 (NGC 2068), vdB 101, vdB 133 and vdB 135 were also taken during the supplemental observing period of *ISO*. These involved full CVF wavelength scans at 5.14 – 9.44 μm (CVF1) and 9.33 – 15.1 μm (CVF2), taken in both the increasing and decreasing wavelength directions, toward each of the source and sky positions. The spectral resolution was $R = 40$. The observations were spaced in wavelength to provide a factor of 1 – 2 oversampling in the vdB 17 and vdB 59 spectra, and 2 – 4 oversampling in those of the other sources. The basic exposure time used was 2.1 s, with 8 exposures per CVF step (totalling 17.6 s) toward the bright sources vdB 17 and vdB 59, and 11 exposures per CVF step (totalling 23.1 s) toward vdB 101, vdB 133 and vdB 135. The pixel scale was 6'' pixel⁻¹ for the vdB 17, vdB 59 and vdB 133 measurements, like that of the earlier position-switched observations, and 12'' pixel⁻¹ for vdB 101 and vdB 135. In this second set of observations, the “source” fields were offset from the central star so as not to contain the star, thus allowing us to use longer integration times without saturating the detector. The vdB 133 field was centered toward the peak IEF emission in the region, as inferred from the earlier position-switched *ISO* observations, and those of vdB 17 and vdB 59 were centered in the directions containing the strongest extended infrared emission in our unpublished near-infrared ground-based images of the regions. The vdB 101 and vdB 135 fields were centered on the same positions observed by Sellgren et al. (1990) in their *IRAS* observations. The sky positions were chosen by examination of the 12 μm *IRAS* skyflux images. Table 3 lists the source and sky positions.

3. Data Reduction

The images were reduced, from the basic (CISP) data product, in the IDL-based ISOCAM data reduction environment known as “ICE”, developed at the Institut d’Astrophysique Spatiale (IAS). By utilizing the basic ICE modules we were able to more

closely monitor and interact with the various stages of processing (i.e., the deglitching of cosmic ray hits from the data, detector transient response rectification and flat-fielding) than with the standard (more automated) CAM IA processing package. Indeed, special efforts were made in the restoration of the source fluxes; the description of the method follows.

3.1. The ISO Camera Transient Response

The ISOCAM detector array experiences a response lag and a flux-dependent transient response (or residual memory effect). In order to recover the actual source fluxes, $I(t)$, models of the detector behavior have been developed by several of the institutes involved with ISOCAM. We have adopted the transient model developed at the IAS (Abergel et al. 1996),

$$M(t) = r I(t) + (1 - r) \int_{-\infty}^t I(t') \exp\left(\frac{t' - t}{\tau(t')}\right) \frac{dt'}{\tau(t')} \quad (1)$$

which has proven from past experience to work best in rectifying low-level flux like that expected of the diffuse nebular emission. The measured flux, M , at time, t , is the sum of the instantaneous response of the detector, $r I(t)$, and the integrated contribution of the exponentially decaying flux history of the detector (Abergel et al 1996). The detector is characterized by two parameters, r and α , the exact behavior of which is not well-known but which likely varies somewhat from pixel to pixel and perhaps with time, over the long term (weeks to months). The time constant for the exponential decay, $\tau = \alpha/M(t)$, is a function both of the measured flux and of the detector parameter, α . In the best of circumstances, the flux history of the detector prior to the start of one’s own observations is known and can then be used to rectify the first part of the flux time series. Since, however, the data prior to one’s own are generally not available, a number of “padding” frames, all with an estimated constant flux value, are instead prepended.

If the detector response were perfect (Figure 1a), the flux history of a 2-cycle chop (sky \rightarrow source \rightarrow sky \rightarrow source) sequence, for a single pixel or an average of pixels in the array, should appear as a series of square functions with the data points falling on two plateaus at a common minimum and two plateaus at a common maximum; the entire pattern then repeats itself (but likely with some general flux offset with respect to the first) for each of the subsequent position-switched cycles taken with a different filter. Figure 1b displays an observed flux time sequence in raw form. The effects of the detector’s finite response time and flux memory are seen to cause significant deviations from the ideal

square pattern. The individual source and sky segments of the flux sequence, which should otherwise have constant levels, are either temporally increasing or decreasing (depending on the history of the detected signal) because of the non-ideal detector behavior.

The position-switched data lend themselves well to the determination of the detector parameters. By using the ideal square-wave pattern as the target in a chi-square minimization procedure, with r , α , and the “padding” constant as free parameters, the best values of these parameters that rectify the observed time sequences can be found. Indeed, a set of parameters was determined for each of the four observation sequences toward vdB133 from averages of those pixels containing the nebular emission. The four parameter sets ranged between $r = 0.72 - 0.73$ and $\alpha = 954 - 1603 \text{ ADU gain}^{-1}$, with padding values of $9.2 - 13.8 \text{ ADU gain}^{-1}$, where ADU gain^{-1} are analog-to-digital units divided by the detector gain. The specific parameter sets were used to rectify the four corresponding vdB133 observation sequences, and their average ($r = 0.72$ and $\alpha = 1200 \text{ ADU gain}^{-1}$) was used to rectify the data sequences of the other sources. The parameter values determined by us provided some improvement over the results based on the values adopted by Abergel et al. (1996), $r = 0.63$ and $\alpha = 1200 \text{ ADU gain}^{-1}$, for observations toward ρ Oph. Figure 1c displays a rectified flux time sequence, after the observed flux time sequence (Fig. 1b) has been rectified using the appropriate parameter values.

In contrast, it is not possible to deduce the detector parameters from the full CVF scans with the method described above, since these scans involve sequential wavelength observations toward a given position and thus do not possess a predictable pattern, much less the regular “square wave” pattern of the position-switched sequences. All full CVF scan sequences of our supplemental observations were thus rectified using the average of the parameters determined from the original vdB133 position-switched sequences: $r = 0.72$ and $\alpha = 1200 \text{ ADU gain}^{-1}$.

The source and sky images were rectified separately before being used to produce the final source – sky maps. In each case, the dark current image (Boulanger 1996) was subtracted from the maps to establish the absolute count levels required for the rectification procedure. It was discovered, however, that the odd-even noise pattern (ISOCAM Team 1994) remained in the images after a simple subtraction of the dark and that multiplication of the dark field (with factors ranging over $1.03 - 1.13$) was needed to eliminate this problem. A single dark multiplication factor was used for all observations of a given source. An uncertainty of $\sim 0.03 \text{ ADU gain}^{-1}$ in determining the dark factor value translates to an uncertainty of $\sim 3 \text{ MJy sr}^{-1}$ in the individual source and sky map levels. However, since the source image and the sky image of a given nebula each use the same dark field (with the same dark multiplicative factor), any errors in absolute flux levels of the component fields

do not propagate into the source – sky maps. The level offset in the source and sky images may lead to differential errors by the rectification process that appear in the source – sky maps, however, on the order of 5% of the absolute sky level (§4).

4. Results

Figures 2, 3, and 4 show our rectified, sky-subtracted spectra of reflection nebulae from position-switched observations and CVF scan observations. Each reflection nebula spectrum is a spatial *average* over a subsection of the image containing the localized IEF emission. The specifics of the spatial subregions used to produce the spectra are given in Table 4. For the position-switched data, where the image contained the illuminating star, the star and the immediately adjacent region containing a spurious arc-like reflection feature from the star (typically pixels X,Y = [6–20, 11–24] of the array) were excluded from the spatial integration.

The position-switched observations were the first performed in this study. The 11 unique wavelength measurements were chosen to measure the strengths of the anticipated Class A interstellar IEFs (6.2, 7.6, 8.62, 11.22 μm), their surrounding continua (4.5, 5.8, 9.5, 10.5, and 15.0 μm) and broad spectral structures such as the 6 – 9 μm bump and the 11 – 13 μm plateau (7.0, 8.4, and 12.0 μm).

The CVF scan observations, which provide a complete CVF spectrum over 5.14 – 15.1 μm , were performed second. In nearly all the CVF scans, there is a strong curvature at the start of the upward and downward scans because of the detector’s flux memory and the satellite having slewed across the bright central star. With such large flux deviations, especially with the case of vdB 17 and vdB 59, the response at the start of each scan could not entirely be corrected by the aforementioned rectification procedures (§3.1). To avoid these transient artifacts, we discarded data shortward of 8.0 μm for the upward scan and data longward of 12.0 μm for the downward scan. Our final sky-subtracted spectra are thus constructed from the downward scan at 5.1 – 8.0 μm , from an average of the upward and downward scans at 8.0 – 12.0 μm , and from the upward scan at 12.0 – 15.1 μm . The difference between the up and down scans is plotted over a slightly wider range of wavelengths for each CVF-scanned spectrum, to estimate the uncertainty in our CVF scan spectra.

The 9 – 10 μm segment of the CVF scan spectra also contain a prominent artifact resulting from the steeply declining transmission functions of the two CVF filter wheels near their wavelength overlap region: the long wavelength extreme of the CVF1 wheel

(5.14 – 9.44 μm) and the short wavelength extreme of the CVF2 wheel (9.33 – 16.52 μm). Thus the 9 – 10 μm spectral region, while shown in some spectra, has been excluded from detailed analysis.

The position-switched spectrum of vdB 133 (Fig 2a) displays the distinct signature of Class A interstellar IEFs at 6.2, 7.6, 8.62, and 11.22 μm . The overwhelming majority of IEF spectra observed fall within this class (Geballe 1997; Tokunaga 1997). The full CVF-scan spectrum (Fig. 2b, and Fig. 1 of Paper I) taken during the supplemental observing period strongly confirms, both in location and relative intensities, the IEFs found in the more coarsely sampled positioned-switched spectrum.

Figure 3 displays the CVF-scanned spectra toward the reflection nebulae vdB 17 and vdB 59. The spectra of both nebulae clearly display the classic 6.2, 7.7, 8.6, 11.3, and 12.7 μm IEFs that characterize Class A type interstellar IEF spectra. Both these nebulae are illuminated by hot, UV-rich stars ($T_{\text{eff}} = 12,000$ K and 19,000 K for vdB 17 and vdB 59, respectively) and are typical of those that display strong interstellar IEFs.

Figure 4 presents 5 – 15 μm spectra of vdB 101, vdB 111, and vdB 135 obtained with ISOCAM. Both the position-switched spectra and the fully-sampled CVF spectra of each source are shown, with the exception of vdB 111, toward which only position-switched observations were made. The fully sampled spectra of vdB 101 and vdB 135 are generally consistent with their position-switched counterparts obtained toward slightly different positions (Table 4). The source and background levels of vdB 101, vdB 111 and vdB 135 measured by ISOCAM at 12 μm are consistent with those of *IRAS*. The reflection nebulae vdB 101, vdB 111, and vdB 135 are all illuminated by cool, UV-poor stars ($T_{\text{eff}} = 5,000$ K, 7,300 K, and 3,600 K, respectively). These three nebulae have very low 12 μm *IRAS* fluxes, ranging between 0.3 and 0.8 MJy sr⁻¹. No IEFs, or continuum emission, are apparent in any of the source – sky spectra above the noise level of the observations, ~ 1 MJy sr⁻¹.

The task of detecting IEFs toward vdB 101, vdB 111, and vdB 135, even with ISOCAM operating under optimal conditions, was understood to be a difficult one. The predicted sensitivity of ISOCAM (~ 0.19 MJy sr⁻¹ with 200s integration time per filter in the position-switched observations) should have been sufficient, in principle. In practice, our actual ISOCAM sensitivity limit was ~ 1 MJy sr⁻¹ for our observations, due to the faintness of the three nebulae compared to the relatively high background emission from diffuse Galactic emission along the same line of sight. The larger than anticipated uncertainty is attributed primarily to the limitations of the rectification procedure to completely correct for the detector effects and the uncertainties in the dark-current subtraction procedure required for the rectification process (discussed in §3). To achieve the expected sensitivity of 0.19 MJy sr⁻¹ on top of a typical background level of 20 MJy sr⁻¹ would require that

our flux rectification procedure be accurate to $\sim 1\%$. Comparison of the upwards and downwards CVF scans indicated that in practice the rectification is only accurate to $\sim 5\%$.

5. Discussion

In the following, we present a quantitative analysis of the IEFs as a function of the UV radiation field. We explore the effect of both the hardness of the UV field (T_{eff} of the illuminating star) and the absolute intensity of the UV field (G_0). We expand our analysis over a wider range of T_{eff} and G_0 by comparing our observed sample to published spectra of vdB 106 (ρ Oph; Boulanger et al. 1996), and vdB 139 (NGC 7023; D. Cesarsky et al. 1996). We also examine spectra at different distances from the illuminating star, for vdB 17 and vdB 59. This examines the effect of constant T_{eff} but varying G_0 .

5.1. Quantifying the UV field toward reflection nebulae

The motivation for our *ISO* observations of reflection nebulae is the observed lack of dependence on T_{eff} of $\Delta\nu I_\nu(12\ \mu\text{m})/I_{\text{bol}}(\text{FIR})$ in reflection nebulae (Sellgren et al. 1990; see §1 and Table 1). This is puzzling because current dust models predict that the *IRAS* 12 μm band is dominated by PAH emission and that PAHs contribute more to the total interstellar extinction curve at UV than visible wavelengths (Désert et al. 1990; Joblin et al. 1992; Siebenmorgen & Krügel 1992; Schutte et al. 1993; Dwek et al. 1997; Li & Greenberg 1997; Silva et al. 1998). Because we are interested in analyzing *ISO* spectra as a function of UV strength, we need to quantify the UV strength in our sources. We have parameterized the UV field in four ways.

Our first method of characterizing the UV field is simply by T_{eff} for the illuminating star of each reflection nebula (Table 1). Hotter stars emit a larger fraction of their total energy in the UV. This is complicated, however, by the difference in T_{eff} for the two stars which illuminate vdB 133 ($T_{\text{eff}} = 6,800\ \text{K}$ and $12,000\ \text{K}$; the cooler star is more luminous).

Another measure of the UV field is the ratio of the stellar flux emitted at UV wavelengths to the total stellar flux. This simplifies the treatment of the UV field in vdB 133, since this ratio equals the sum of the UV fluxes of the two stars divided by the sum of the total flux of the two stars. The relationship between T_{eff} and the ratio of UV to total stellar flux is, however, defined by the longest wavelength included in the range of UV wavelengths. We have explored two ranges of UV wavelengths, both inspired by previous theoretical, observational, and laboratory work on PAHs and the IEFs.

The low ratio of visible to UV absorption, for the distribution of PAH sizes included in published models of interstellar absorption and emission, occurs because large molecules in general do not have electronic transitions beyond a cutoff wavelength, λ_{cutoff} , proportional to the molecule’s length (Platt 1956). Values of $\lambda_{\text{cutoff}} = 300 - 500$ nm have been estimated for neutral PAHs containing roughly 40 carbon atoms (Crawford, Tielens, & Allamandola 1985; Allamandola et al. 1989; Léger et al. 1989; Désert et al. 1990; Joblin et al. 1992; Schutte et al. 1993). Ionized PAHs absorb at longer wavelengths than their neutral counterparts (Salama et al. 1996 and references therein). Approximate formulae for the relation between λ_{cutoff} and PAH size have been published for neutral PAHs (Désert et al. 1990; Schutte et al. 1993) and for ionized PAHs (Désert et al. 1990; Salama et al. 1996).

Thus, as our second method of parameterizing the UV field, we define a UV wavelength range of 91 – 400 nm. In this case, the fraction of total stellar flux emitted at UV wavelengths is $F_{(\lambda < 400\text{nm})}/F_{\text{total}}$. We chose $\lambda_{\text{cutoff}} = 400$ nm for this definition because it corresponds to the value of λ_{cutoff} , averaged over a distribution of PAH sizes and charge, at which current dust models predict the contribution of PAHs to the total interstellar extinction curve becomes negligible (Désert et al. 1990; Joblin et al. 1992; Siebenmorgen & Krügel 1992; Dwek et al. 1997; Silva et al. 1998). Note 400 nm falls just longward of the observational dividing line between UV and visible wavelengths.

Our third method of parameterizing the UV field is to define a UV wavelength range of 91 – 240 nm. Many previously published theoretical and observational papers on the ISM characterize the ambient radiation field by G_0 , the strength of the 91 – 240 nm UV radiation field. Examples of the prevalence of G_0 as a measure of the UV energy density include observational and theoretical studies of the 12 μm *IRAS* emission in our own and other galaxies (Draine & Anderson 1985; Ryter, Puget, & Pérault 1987; Boulanger et al. 1988; Désert et al. 1990; Helou, Ryter, & Soifer 1991; Rowan-Robinson 1992), analysis of the observed strengths of the IEFs from recent *ISO* and *IRTS* spectra (Boulanger et al. 1996, 1998a, 1998b; Onaka 1999), and models exploring the ionization state of PAHs and their effect on the heating and chemistry of different regions of the ISM (Allamandola et al. 1989; Bakes & Tielens 1994, 1998; Spaans et al. 1994; Wolfire et al. 1995; Salama et al. 1996; Dartois & d’Hendecourt 1997). For a UV range of 91 – 240 nm, the fraction of total stellar flux emitted at UV wavelengths is $F_{(\lambda < 240\text{nm})}/F_{\text{total}}$.

Figure 5 displays $F_{(\lambda < 400\text{nm})}/F_{\text{total}}$ and $F_{(\lambda < 240\text{nm})}/F_{\text{total}}$ as a function of T_{eff} , determined using two different stellar models. We use Kurucz (1979) stellar atmospheric models for $T_{\text{eff}} > 5,500$ K, with $\log(g) = 4.0$. We find, however, that the results are not sensitive to the value of $\log(g)$ adopted. Since the Kurucz models do not extend to cooler temperatures, we use a blackbody (Planck) function to model stars with $T_{\text{eff}} < 5,500$ K. Figure 5 shows that a

blackbody slightly overestimates $F_{(\lambda < 400\text{nm})}/F_{total}$ and $F_{(\lambda < 240\text{nm})}/F_{total}$ for the coolest stars for which we have Kurucz models. Figure 5 and Table 1 show that $F_{(\lambda < 400\text{nm})}/F_{total}$ drops by a factor of 10, and $F_{(\lambda < 240\text{nm})}/F_{total}$ falls by over a factor of 100, as T_{eff} decreases from 21,000 K to 5,000 K.

Our fourth method of parameterizing the UV field incident on a particular nebular position is by G_0 (sometimes called χ or u), the strength of the 91 – 240 nm UV radiation field in units of the local interstellar radiation field. A value of $G_0 = 1$ corresponds to a UV radiation field of $1.6 \times 10^{-3} \text{ erg s}^{-1} \text{ cm}^{-2}$ at $\lambda = 91 - 240 \text{ nm}$ (Habing 1968). Table 5 presents the distance to each source and the projected angular separation between the illuminating stars and the observed nebular region used to derive G_0 . A single value of G_0 suffices for vdB 106, vdB 133, and vdB 139, where the observed spectrum was obtained over a narrow range of distances from the central star, and for vdB 101, vdB 111, and vdB 135, which we did not detect with *ISO* spectroscopy. For vdB 17 and vdB 59, we were able to obtain spectra at a range of values of stellar distance and thus G_0 . Table 5 gives the value of G_0 at a typical nebular position for these two nebulae; we discuss how the spectra of vdB 17 and vdB 59 depend on nebular position (and thus G_0) in a later section.

We summarize the UV field for our observed sources and published comparison sources, as measured by T_{eff} , $F_{(\lambda < 400\text{nm})}/F_{total}$, $F_{(\lambda < 240\text{nm})}/F_{total}$, and G_0 , in Tables 1 and 5. The observed values of $\Delta\nu I_\nu(12 \mu\text{m})/I_{\text{bol}}(\text{FIR})$ (Sellgren et al. 1990; see §1 and Table 1) are independent of *all* these measures of the UV strength.

5.2. PAH ionization state in reflection nebulae

Another reason to quantify the UV field in reflection nebulae is to search for spectroscopic differences between neutral and ionized PAHs. Interstellar PAHs are predicted to be mainly positively charged and neutral in reflection nebulae illuminated by B stars, and mainly neutral and negatively charged in the diffuse interstellar medium (Bakes & Tielens 1994, 1998; Salama et al. 1996; Dartois and d’Hendecourt 1997). Predicted differences between neutral and ionized PAHs include changes both in the central wavelengths and in the relative strengths of PAH features (De Frees et al. 1993; Szczepanski & Vala 1993; Hudgins, Sandford, & Allamandola 1994; Pauzat, Talbi, & Ellinger 1995, 1997; Langhoff 1996; Cook & Saykally 1998; Allamandola, Hudgins, & Sandford 1999; Hudgins & Allamandola 1999b).

The first ionization potential of PAHs lies in the range 4 – 8 eV, with a tendency for the ionization potential to decrease with increasing PAH size (Bakes & Tielens 1994; Salama et al. 1996). Hudgins & Allamandola (1999a) conclude from the wavelength spacing of the 6.2

and 7.7 μm IEFs observed in the ISM that these IEFs arise from ionized PAHs with 50 – 80 carbon atoms. A PAH with 50 – 80 carbon atoms has a first ionization potential of 5.8 – 6.2 eV, corresponding to an ionization wavelength of 200 – 210 nm (Bakes & Tielens 1994). The value of G_0 (with $\lambda_{\text{cutoff}} = 240$ nm) is thus a rough indicator of the intensity of stellar radiation capable of ionizing PAHs at any given nebular position.

Theory predicts that the mean ionization state of interstellar PAHs is a function of G_0 (Bakes & Tielens 1994, 1998; Salama et al. 1996; Dartois and d’Hendecourt 1997). If the spectral features we observe in reflection nebulae are due to PAHs, then we would expect to detect changes both in the central wavelengths and in the relative strengths of IEFs between nebulae with different values of G_0 . One goal of our observations is to test this prediction.

5.3. Spatially averaged reflection nebulae spectra

Localized enhancements of IEF emission, at 6.2, 7.7, 8.6, 11.3, and 12.7 μm , were detected in the source – sky spectra in three of the six nebulae observed: vdB 17, vdB 59 and vdB 133. These three nebulae are illuminated by the hotter stars in our sample, with $T_{\text{eff}} = 6,800$ K – 19,000 K. Our ~ 1 MJy sr^{-1} upper limits on the IEF emission in vdB 101, vdB 111, and vdB 135 are consistent with their 12 μm *IRAS* surface brightnesses of 0.3 – 0.8 MJy sr^{-1} (Sellgren et al. 1990). These faint nebulae have cooler illuminating stars, with $T_{\text{eff}} = 3,600$ K – 7,300 K.

Figure 6 displays the superposed spectra of vdB 17, vdB 59, and vdB 133, those nebulae we observe having IEF emission in excess of the adjacent sky emission. These spectra (from Figs. 2 and 3) are spatial averages over the emission region in each reflection nebula, defined by visual inspection of the images. Each spectrum is scaled by its average intensity over the 12 μm *IRAS* band ($\lambda \simeq 7.5 - 15$ μm). We choose this scaling to illustrate the IEF peak and continuum levels (in MJy sr^{-1}), normalized to an *IRAS* 12 μm intensity of 1 MJy sr^{-1} , for typical reflection nebulae. Such illustration is useful for planning for future mid-infrared spectroscopy with *SIRTF* and *SOFIA* of sources detected by the *IRAS* all-sky survey.

The reflection nebulae spectra in Figure 6, including their continua, broad emission bumps, and narrow IEFs, are roughly similar in shape despite the widely varying range of conditions quantified in Tables 1 and 5. The normalized peak fluxes of the different IEFs vary by less than a factor of two from source to source. More importantly, these variations show no systematic dependence on T_{eff} . No evidence is seen among these three spectra for

disappearance of IEFs, appearance of new spectral features, shifts in IEF wavelengths, or dramatic changes in the strengths of IEFs relative to the broad emission bumps or the continuum emission.

5.3.1. Quantifying the IEF Features

The quantitative fluxes of the narrow IEFs, broad emission bumps, and continuum are quite sensitive to how the spectrum is divided into separate spectral components. Figure 7 displays the spectrum of vdB 17, to illustrate the range of possibilities for dividing the emission between the different spectral components.

Figure 7a shows Method 1, in which we simultaneously fit Gaussians to the five *narrow* IEFs (at 6.2, 7.7, 8.6, 11.3 and 12.7 μm) and to two *broad* emission features at ~ 7 and 12 μm . The latter two features represent the 6 – 9 μm “bump” (Cohen et al. 1986; Bregman et al. 1989) and the 11 – 13 μm “plateau” (Cohen, Tielens, & Allamandola 1985). The *continuum* is approximated by a spline fit through the data points at ~ 5.4 , 10.3, and 14.8 μm . The central wavelengths, widths, and heights of the Gaussians were all free parameters in the fit. Boulanger et al. (1998a) have suggested that the IEFs are best fit by Lorentzians. We used Gaussians rather than Lorentzians for the IEFs because they provide a better spectral fit to the IEFs observed in NGC 7023 at $R = 1000$ (Sellgren et al. 1999).

Figure 7b shows Method 2, in which we simultaneously fit Gaussians to the five narrow IEFs (at 6.2, 7.7, 8.6, 11.3 and 12.7 μm). The continuum is modeled by a spline fit to all spectral data points outside that of the narrow IEFs; we assume the broad emission features at 6 – 9 μm and at 11 – 13 μm are not distinct from the continuum but rather are simply undulations in the continuum level in this case. Again the central wavelengths, widths, and heights of the Gaussians are free parameters in the fit.

Figure 7c shows Method 3, in which we modeled the continuum by a linear fit to the spectral data points at ~ 5.3 and 15.0 μm , the wavelength extremes of the observations. No broad emission features are assumed in this case. The fluxes of the five narrow IEFs were found by directly integrating over the continuum-subtracted spectra, the method most used in previous studies. The integration limits adopted for the 6.2, 7.7, 8.6, 11.3 and 12.7 μm lines were (6.0 – 6.6 μm), (7.2 – 8.1 μm), (8.1 – 9.9 μm), (10.5 – 12.0 μm), (12.0 – 13.5 μm), respectively, as indicated in Figure 7c. The limits of the 6.2, 7.7, 8.6, and 11.3 μm IEFs are those used by Lu (1998). For the 12.7 μm IEF, which Lu does not include in his analysis, we integrate over a wavelength range similar in extent ($\Delta\lambda = 1.5 \mu\text{m}$) to that used for the 11.3 μm line.

Figure 7 illustrates the sensitivity of the estimated strengths of IEFs, broad features, and continuum to whether Method 1, 2, or 3 is used to fit the spectrum. The Gaussian used to fit the 6 – 9 μm broad bump in Method 1 is centered near 6.7 μm , and as a result the narrow 7.7 μm IEF and especially the 8.6 μm IEF appear stronger. The higher adopted continuum level at 6 – 9 μm in Method 2 is centered closer to 7.5 μm , which results in a somewhat weaker 7.7 μm IEF and a much weaker 8.6 μm IEF. The choice of a linear continuum (fitted to points at 5.3 and 15.0 μm) in Method 3 consistently produce the highest 6 – 9 μm feature strengths of among the methods. The choice of broad integration limits for the 8.6 μm feature (8.1 – 9.9 μm) result in strengths comparable to or exceeding that of the 6.2 μm feature. Method 2 and Method 3 represent two extremes for the treatment of the 6 – 9 μm region.

Previous studies of the relative strengths of different IEFs vary in their choices of continuum placement and integration limits in wavelength; the choice of continuum by Cohen et al. (1986, 1989) and Lu (1998) in their analyses is similar to Method 2, while that of Jourdain de Muizon, d’Hendecourt, & Geballe (1990) and Zavagno, Cox, & Baluteau (1992) is more like that of Methods 1 and 3. The sensitivity of our feature strengths to continuum placement, especially, demonstrates how much care must be exercised in intercomparing the results of different studies.

5.3.2. Comparison of Nebulae

Table 6 presents our quantitative results for the strengths of the IEFs, broad emission features, and continuum in vdB 17, vdB 59, vdB 133 (Paper I), vdB 139 (NGC 7023; D. Cesarsky et al. 1996), and vdB 106 (ρ Oph; Boulanger et al. 1996) derived by three different methods for defining the IEFs and continuum. The methods by which the continuum and IEFs are defined, and thus the feature ratios quoted, vary between studies; the three methods employed here are representative of those typically used. The individual feature strengths are given in units of integrated line flux ($\text{ergs s}^{-1} \text{cm}^{-2} \text{sr}^{-1}$) divided by the total integrated 11.3 μm line flux (in $\text{ergs s}^{-1} \text{cm}^{-2} \text{sr}^{-1}$).

Table 6 shows that the relative strengths we derive for the IEFs, broad emission features, and continuum emission are very similar for all the sources we analyze, within a given method for decomposing the spectrum. The relative IEF strengths for any given source, however, are very sensitive to the method chosen. Figure 8 illustrates this with the 8.6 to 11.3 μm IEF ratio, $I(8.6 \mu\text{m})/I(11.3 \mu\text{m})$, plotted against T_{eff} . We originally chose this ratio because it is predicted to be much stronger for ionized PAHs than for neutral PAHs (De Frees et al. 1993; Szczepanski & Vala 1993; Hudgins et al. 1994; Pauzat et al. 1995,

1997; Langhoff 1996; Cook & Saykally 1998; Allamandola et al. 1999; see §5.4.1). The value of T_{eff} (Table 1) is a measure of the hardness of the UV radiation field, which is independent of any adopted value of λ_{cutoff} , and which should be similar for all nebular positions included in the spatially averaged spectrum of each source. Figure 8 shows, however, that systematic differences in the mean values of $I(8.6 \mu\text{m})/I(11.3 \mu\text{m})$, measured by Methods 1, 2, and 3, are much larger than the source-to-source scatter of $I(8.6 \mu\text{m})/I(11.3 \mu\text{m})$ for any particular method.

5.3.3. Convolution of the Spectra with Broad-band Filters

Much effort has gone into characterizing the mid-infrared emission of the ISM using broadband filters, which provide limited spectral information but higher sensitivity than narrowband filters or spectrometers. The entire sky has been surveyed in the *IRAS* 12 μm filter, and many ISOCAM studies have been conducted with the LW2 and LW3 filters, centered at 6.75 and 15 μm respectively. Note that the ISOCAM LW10 filter and the ISOPHOT 11.5 μm filter are designed to be the same as the *IRAS* 12 μm filter. Each of these broad filter bandpasses covers a mixture of IEFs, broad emission features, and continuum emission from interstellar dust and molecules. Table 6 therefore presents the expected *IRAS* 12 μm source fluxes and ISOCAM LW 2 source fluxes found by convolving the source spectra with the 12 μm *IRAS* band transmission profile and LW 2 transmission profile (Fig. 7d), respectively.

We have also investigated what fraction of the flux within these broadband filters comes from each spectral component in the reflection nebulae we have observed. Table 7 gives the relative contributions of the IEFs, broad emission features, and continuum to the broadband fluxes measured with broadband filters in common use. We derived these results by convolving the ISOCAM CVF spectra with the transmission profile of the LW2 (6.75 μm) filter on ISOCAM and the *IRAS* 12 μm filter. Again, we find the estimated percentage contributions of IEFs, broad features, and continuum to the *IRAS* 12 μm filter and the ISOCAM LW2 filter are remarkably consistent from nebula to nebula, within a given Method (1, 2, or 3), but the absolute values for any nebula are quite sensitive to which Method (1, 2, or 3) is used to fit the spectrum. The choice of the continua via Method 3 gives the maximal values of the narrow IEF/total ratios, while those of Method 2 represent the lower extreme. For the *IRAS* 12 μm filter, the narrow IEFs contribute typically $\sim 20\%$ (Method 1), $\sim 40\%$ (Method 2), and $\sim 60\%$ (Method 3) of the total flux depending on the method used to define the continuum. All methods imply that 40 – 80% of the *IRAS* 12 μm flux is due to continuum emission and/or broad emission features, rather than the narrow

IEFs.

5.4. Spatial variations within individual reflection nebulae

The spectra for vdB 17 and vdB 59 plotted in Figures 3 and 6, and analyzed in Figures 7 and 8 and Table 6, have been integrated over a wide range of projected distance from the central star. In this next section we explore how the spectral features within a single source image depend on position for vdB 17 and vdB 59.

We have divided the spectrophotometric images of vdB 17 and 59 into radial bins, characterizing each bin by the incident UV starlight, G_0 . We scale the values of G_0 in Table 5 by the inverse square of the projected angular separation of each pixel from the illuminating star. Figure 9 shows the average spectra of different radial bins within vdB 17 and vdB 59. The values of G_0 in these bins are equally spaced in $\log(G_0)$; they vary over $G_0 = 20 - 4 \times 10^3$ for vdB 17, and over $G_0 = 200 - 6 \times 10^4$ for vdB 59.

Near-infrared long-slit spectroscopy of vdB 17 and 59 (Martini, Sellgren, & DePoy 1999), as well as our unpublished ground-based near-infrared imaging and the *ISO* images we analyze here, suggest that vdB 17 has a much simpler geometry than vdB 59. Thus our use of the projected distance between a pixel and the central star to estimate G_0 for each pixel is likely to be a better approximation for vdB 17 than for vdB 59.

Figure 9 shows interesting variations in the spectra of vdB 17 as a function of nebular position (or G_0). At first glance, it appears that the 8.6 μm IEF steadily becomes less prominent in the spectra at low values of G_0 . A more careful examination, however, shows that the *peak* intensity of the 8.6 μm IEF, relative to the peak intensity of the 7.7 μm IEF, is relatively constant with G_0 . Instead, it seems that the apparent weakening of the 8.6 μm IEF at low G_0 is rather due to a broadening of the overlapping 7.7 μm IEF.

Figure 10 quantifies the change in the full-width at half-maximum (FWHM) of the 7.7 μm IEF with G_0 in vdB 17. We adopted the method of Boulanger et al. (1998a) to measure the FWHMs of different IEFs, by fitting a linear baseline to continuum points near 5 and 15 μm , and then fitting a blend of three Lorentzians to the 6.2, 7.7, and 8.6 μm IEFs. Figure 10 clearly shows that the 7.7 μm IEF is systematically broader at low values of G_0 in vdB 17. Figure 10 also suggests that perhaps the 6.2 μm IEF may also broaden with lower G_0 , but the evidence is not as compelling as it is for the 7.7 μm IEF. No change in the FWHM of the 8.6 μm IEF is observed within the uncertainties.

The spectra of vdB 59, in contrast to those of vdB 17, do not show any strong systematic

dependence on G_0 . The width of the 7.7 μm IEF and the contrast of the 8.6 μm IEF against the red wing of the 7.7 μm IEF show little change in Figure 9. This may be due to the more complex geometry of vdB 59, where emission from regions close to and far from the star appear to contribute to the same line of sight (Martini et al. 1999). Alternatively, this may be because G_0 in vdB 59 does not extend to the low values ($G_0 = 20 - 60$) where the most marked spectral changes are observed in vdB 17.

The origin of the widths of the IEFs is quite controversial and this complicates any explanation of why the 7.7 μm IEF width changes spatially within vdB 17. An increase in PAH temperature should broaden the IEFs, but that would also result in a shift in the IEF central wavelengths (Joblin et al. 1995). We, however, do not observe any such shift in the 7.7 μm IEF central wavelength. An increase in particle size might broaden the IEFs (Boulanger et al. 1998). A change in the mix of the IEF emitters, all of which have slightly different wavelengths, could also lead to a change in the IEF widths (Cook & Saykally 1998; Le Coupanec et al. 1998; Papoular 1999). Other broadening mechanisms are discussed by the above authors; whichever mechanism accounts for the broadening of the 7.7 μm IEF that we observe in vdB 17 needs to be consistent with the much lower, or non-existent, broadening we observe in the 6.2 and 8.6 μm IEFs, and with the constancy in the central wavelengths of all the observed IEFs.

The *peak* strengths of the 6.2 and 8.6 μm IEFs, relative to the peak strength of the 7.7 μm IEF, show little variation among spectra at different distances within vdB 17 and vdB 59, over $G_0 = 20 - 6 \times 10^4$ (Fig. 9). The peak intensity of the 8.6 μm IEF of vdB 17, relative to the peak intensity of the 7.7 μm IEF, has values of 0.53 – 0.56 in Figure 9. A similar constancy in peak intensity (relative to the peak 7.7 μm IEF intensity) is observed for the 8.6 μm IEF within vdB 59 and for the 6.2 μm IEF within both vdB 17 and vdB 59.

Figure 9 also shows marginal evidence for a weak emission feature near 6.9 μm appearing in the spectra of one or two of the most distant radial bins within vdB 17. A weak interstellar emission feature at 6.9 μm was first discovered by Bregman et al. (1983) and further analyzed by Cohen et al. (1986). This emission feature can be confused with [Ar II] emission at 7.0 μm , and so can only be reliably detected at low spectral resolution in sources free of ionized hydrogen, such as reflection nebulae. The 6.9 μm feature is not detected in spectra of radial bins closer to the star in vdB 17 (Fig. 9). The 6.9 μm feature is also not detected in the spectra of any radial bin for vdB 59 (Fig. 9), or in the spatially integrated *ISO* spectra of vdB 17 or vdB 59 (Fig. 3), vdB 133 (Fig. 2; Paper I), vdB 139 (NGC 7023; D. Cesarsky et al. 1996; Laureijs et al. 1996) or vdB 106 (ρ Oph; Boulanger et al. 1996). The 0–0 S(5) H_2 line at 6.9 μm is unlikely to be a contributor, as other H_2 lines with similar predicted strengths, at 8.0, 9.7, and 12.3 μm , are not detected, and because the 1–0 S(1) H_2

emission in our unpublished narrowband images of vdB 17 is concentrated near the star at higher G_0 values. We are therefore cautious in claiming that we have detected $6.9 \mu\text{m}$ emission in the outermost regions of vdB 17.

5.4.1. *The $8.6 \mu\text{m}$ emission feature*

Laboratory data and theoretical calculations for PAHs show that the 8.6 to $11.3 \mu\text{m}$ IEF flux ratio, $I(8.6 \mu\text{m})/I(11.3 \mu\text{m})$, is much higher in ionized than neutral PAHs (De Frees et al. 1993; Szczepanski & Vala 1993; Hudgins et al. 1994; Pauzat et al. 1995, 1997; Langhoff 1996; Cook & Saykally 1998; Allamandola et al. 1999). The $8.6 \mu\text{m}$ and $11.3 \mu\text{m}$ bands in PAHs correspond to the in-plane bend and out-of-plane bend, respectively, of the same aromatic C–H bond. Thus $I(8.6 \mu\text{m})/I(11.3 \mu\text{m})$ should be a useful measure of PAH ionization because it should be less sensitive to PAH size or PAH hydrogenation than the ratio of an aromatic C–C vibration to an aromatic C–H vibration.

The mean PAH ionization is predicted to increase with G_0 (Bakes & Tielens 1994, 1998; Salama et al. 1996; Dartois and d’Hendecourt 1997). One test of the PAH hypothesis, therefore, is to measure $I(8.6 \mu\text{m})/I(11.3 \mu\text{m})$ as a function of G_0 . Joblin et al. (1996) have observed $I(8.6 \mu\text{m})/I(11.3 \mu\text{m})$ to increase closer to the star in the reflection nebula NGC 1333/SVS-3. They interpret this as due to PAHs becoming increasingly ionized near the B-type illuminating star.

Figures 7, 8, and Table 6, however, demonstrate how strongly the measured value of $I(8.6 \mu\text{m})/I(11.3 \mu\text{m})$ in our data depends on the method used to separate the $8.6 \mu\text{m}$ IEF from other spectral components such as the $7.7 \mu\text{m}$ IEF and the $6 - 9 \mu\text{m}$ broad emission bump. A local baseline (Method 2) to measure the strength of the $8.6 \mu\text{m}$ IEF would lead us to conclude that the $8.6 \mu\text{m}$ IEF virtually disappears at low values of G_0 in vdB 17, as can be seen qualitatively in Figure 9. The observed broadening of the $7.7 \mu\text{m}$ IEF at low G_0 in vdB 17 (Figure 10) will, however, cause an increase in strength in the wing of the $7.7 \mu\text{m}$ IEF. Because the red wing of the $7.7 \mu\text{m}$ IEF defines the local continuum for the $8.6 \mu\text{m}$ IEF in Method 2, any broadening of the $7.7 \mu\text{m}$ IEF (at constant $7.7 \mu\text{m}$ peak intensity) naturally results in an apparent weakening in the $8.6 \mu\text{m}$ IEF strength measured by this method. When we treat the 7.7 and $8.6 \mu\text{m}$ IEFs as a blend of two symmetrical features lying above a much lower continuum level (Method 1), then we find that the $8.6 \mu\text{m}$ IEF shows little variation with G_0 in vdB 17.

We conclude that $I(8.6 \mu\text{m})/I(11.3 \mu\text{m})$ is extremely dependent on how the $8.6 \mu\text{m}$ IEF is measured (Figs. 7 and 8; Table 6). Joblin et al. (1996) use a local baseline (Method 2)

in measuring the strength of the 8.6 μm IEF, because their ground-based spectra do not extend to short enough wavelengths to include the entire 7.7 μm IEF. The increase in the 7.7 μm IEF width with decreasing G_0 we observe in vdB 17 (Figs. 9 and 10) leads us to urge caution in using $I(8.6 \mu\text{m})/I(11.3 \mu\text{m})$ to quantify PAH ionization.

5.4.2. The ratio of 6 – 10 μm emission to 10 – 14 μm emission

The difficulty of quantifying the observed 8.6 μm IEF strength inspires us to search for a more robust way to test predictions of the PAH ionization state as a function of G_0 . Laboratory data and theoretical calculations for PAHs show that the sum of all the PAH bands at 6 – 10 μm , relative to the sum of all the PAH bands at 10 – 14 μm , is at least an order of magnitude higher in ionized PAHs than in neutral PAHs (De Frees et al. 1993; Szczepanski & Vala 1993; Hudgins et al. 1994; Pauzat et al. 1995, 1997; Langhoff 1996; Cook & Saykally 1998; Allamandola et al. 1999). We therefore have measured $I(5.50\text{--}9.75 \mu\text{m})/I(10.25\text{--}14.0 \mu\text{m})$, the ratio of the integrated intensity at 5.50 – 9.75 μm to the integrated intensity at 10.25 – 14.0 μm , in *ISO* spectra of reflection nebulae, as an alternate way to search for the spectroscopic signature of changing PAH ionization state.

Figure 11 presents our measurements of $I(5.50\text{--}9.75 \mu\text{m})/I(10.25\text{--}14.0 \mu\text{m})$ as a function of G_0 in reflection nebulae. We subtracted a continuum from each spectrum before measuring $I(5.50\text{--}9.75 \mu\text{m})/I(10.25\text{--}14.0 \mu\text{m})$. The 5.50 – 9.75 μm continuum was defined by a linear fit to data points near 5.3 and 10.0 μm . The 10.25 – 14.0 μm continuum was defined by a linear fit to data points near 10.0 and 14.5 μm . We plot a single value of $I(5.50\text{--}9.75 \mu\text{m})/I(10.25\text{--}14.0 \mu\text{m})$ for vdB 106 (ρ Oph; Boulanger et al. 1996), vdB 133 (Fig. 2b and Paper I), and vdB 139 (NGC 7023; D. Cesarsky et al. 1996). For vdB 17 and vdB 59, we plot $I(5.50\text{--}9.75 \mu\text{m})/I(10.25\text{--}14.0 \mu\text{m})$ at six values of G_0 , derived from the spectra of the radial bins shown in Figure 9.

The remarkable conclusion from Figure 11 is that $I(5.50\text{--}9.75 \mu\text{m})/I(10.25\text{--}14.0 \mu\text{m})$ changes by no more than 40% among sources with $G_0 = 20 - 6 \times 10^4$. This observational ratio should not depend at all on how the observed interstellar spectra are divided into separate narrow IEFs and broader emission components. We emphasize that $I(5.50\text{--}9.75 \mu\text{m})/I(10.25\text{--}14.0 \mu\text{m})$ should be a more robust and sensitive measure of the PAH ionization state than $I(8.6 \mu\text{m})/I(11.3 \mu\text{m})$.

Our observation that the mid-infrared spectra of vdB 17 and vdB 59 are very similar for $G_0 = 20 - 6 \times 10^4$ (Figs. 9 and 11) are in strong agreement with other recent work. Boulanger et al. (1998b) concludes that the IEF flux ratios in *ISO* spectra of the

Chamaeleon cloud, the ρ Oph cloud, NGC 7023, and M17 show no systematic dependence on G_0 , over $G_0 = 1 - 10^5$. Onaka (1999) finds that the IEF flux ratios in *ISO* spectra of the Carina nebula are independent of G_0 , over $G_0 = 100 - 10^5$.

6. Conclusions

We have obtained 5 – 15 μm ISOCAM CVF spectroscopy of six reflection nebulae, in order to test predictions of interstellar models for the infrared emission features. Our sample includes a range of UV field hardness ($T_{\text{eff}} = 3,600 \text{ K} - 19,000 \text{ K}$ for the illuminating stars; $F_{(\lambda < 400\text{nm})}/F_{\text{total}} = 0.01 - 0.87$) and UV field intensity ($G_0 = 20 - 6 \times 10^4$).

Our first goal was to search for spectroscopic differences as a function of T_{eff} for the illuminating stars. Detection of such spectroscopic differences could potentially reconcile 12 μm broad-band *IRAS* observations showing that $\Delta\nu I_\nu(12 \mu\text{m})/I_{\text{bol}}(\text{FIR})$ is independent of T_{eff} , for reflection nebulae illuminated by stars $T_{\text{eff}} = 5,000 - 33,000 \text{ K}$ (Sellgren et al. 1990), with model predictions that the *IRAS* 12 μm emission is dominated by PAHs which contribute much more to the total interstellar extinction curve at UV wavelengths than at visible wavelengths (Désert et al. 1990; Joblin et al. 1992; Siebenmorgen & Krügel 1992; Dwek et al. 1997; Silva et al. 1998).

A second goal was to search for spectroscopic differences as a function of G_0 . Interstellar models predict that more PAHs are positively charged when G_0 increases (Bakes & Tielens 1994, 1998; Salama et al. 1996; Dartois and d’Hendecourt 1997). Laboratory data and theoretical calculations for PAHs show that $I(8.6 \mu\text{m})/I(11.3 \mu\text{m})$ and $I(5.50\text{--}9.75 \mu\text{m})/I(10.25\text{--}14.0 \mu\text{m})$ are both much higher in ionized than neutral PAHs (De Frees et al. 1993; Szczepanski & Vala 1993; Hudgins et al. 1994; Pauzat et al. 1995, 1997; Langhoff 1996; Cook & Saykally 1998; Allamandola et al. 1999).

We detect *interstellar* IEFs at 6.2, 7.7, 8.6, 11.3, and 12.7 μm , broad emission features at 6 – 9 μm and 11 – 13 μm , and continuum emission at 5 – 15 μm in the reflection nebulae vdB 17, vdB 59, and vdB 133. These nebulae were the brightest in our sample and illuminated by hotter stars ($F_{(\lambda < 400\text{nm})}/F_{\text{total}} = 0.22 - 0.87$). The normalized peak fluxes of the different IEFs vary by less than a factor of two among these three nebulae, with no systematic dependence on T_{eff} . No evidence is seen among these spectra for disappearance of IEFs, appearance of new spectral features, shifts in IEF wavelengths, or dramatic changes in the strengths of IEFs relative to the broad emission bumps or the continuum emission.

We do not detect any feature emission or continuum emission in vdB 101, vdB 111, and vdB 135. These nebulae were the faintest in our sample and were illuminated by cooler

stars ($F_{(\lambda < 400\text{nm})}/F_{total} = 0.01 - 0.20$). Their upper limits are consistent with their low measured $12\ \mu\text{m}$ *IRAS* surface brightnesses.

We compare spatially averaged spectra of vdB 17, vdB 59, and vdB 133 to published spectra of vdB 106 (ρ Oph; Boulanger et al. 1996) and vdB 139 (NGC 7023; D. Cesarsky et al. 1996). Qualitative comparison of spectra show all these spectra are very similar over a range of UV hardness ($T_{\text{eff}} = 6,800 - 22,000$; $F_{(\lambda < 400\text{nm})}/F_{total} = 0.22 - 0.92$) and UV intensity ($G_0 = 40 - 1800$).

We find that quantifying the IEF fluxes is quite sensitive to the method by which the spectra are separated into IEFs, broad emission bumps, and continuum. For instance, $I(8.6\ \mu\text{m})/I(11.3\ \mu\text{m})$ shows no dependence on T_{eff} for any given method of defining the IEF fluxes, but $I(8.6\ \mu\text{m})/I(11.3\ \mu\text{m})$ shows strong systematic differences between the values derived by different methods.

We also quantify the contributions of IEFs, broad emission bumps, and continuum to broad-band filters such as the *IRAS* $12\ \mu\text{m}$ filter and the ISOCAM LW 2 ($6.75\ \mu\text{m}$) filter. Again, for any given method of distinguishing between these separate spectral components, the contributions of each component to the broad-band filters are independent of T_{eff} , but the absolute value of the contribution depends strongly on the method for how the spectrum is divided among IEFs, broad emission bumps, and continuum.

We divide the spectra of vdB 17 and vdB 59 into radial bins, with the UV field of each bin characterized by G_0 . We find that the *peak* intensities of the 6.2 and $8.6\ \mu\text{m}$ IEFs, compared to the peak intensity of the $7.7\ \mu\text{m}$ IEF, show no variation over $G_0 = 20 - 6 \times 10^4$ in vdB 17 and vdB 59.

In the most distant regions of vdB 17, we observe that the $8.6\ \mu\text{m}$ IEF appears weaker due to increased blending with the $7.7\ \mu\text{m}$ IEF. We quantify the FWHM of the $7.7\ \mu\text{m}$ feature, and find that it grows systematically broader at low G_0 in vdB 17. We conclude that the low contrast of the $8.6\ \mu\text{m}$ IEF at low G_0 in vdB 17 is the result of the increased width of the $7.7\ \mu\text{m}$ IEF. This observed broadening of the $7.7\ \mu\text{m}$ IEF, combined with the sensitivity of $I(8.6\ \mu\text{m})/I(11.3\ \mu\text{m})$ to baseline placement for the $8.6\ \mu\text{m}$ IEF, suggests that caution should be used in inferring PAH ionization from $I(8.6\ \mu\text{m})/I(11.3\ \mu\text{m})$.

We suggest using $I(5.50-9.75\ \mu\text{m})/I(10.25-14.0\ \mu\text{m})$ as an alternate method of testing the predictions of PAH ionization as a function of G_0 . We measure this in single nebular positions in vdB 106, vdB 133, and vdB 139 and at different nebular positions within vdB 17 and vdB 59. We observe that $I(5.50-9.75\ \mu\text{m})/I(10.25-14.0\ \mu\text{m})$ decreases by no more than 40% over $G_0 = 20 - 6 \times 10^4$.

Our observational results are in strong agreement with Boulanger et al. (1998b), who concludes that the IEF flux ratios in *ISO* spectra of the Chamaeleon cloud, the ρ Oph cloud, NGC 7023, and M17 show no systematic dependence on G_0 over $G_0 = 1 - 10^5$. Our results also strongly support Onaka (1999), who finds that the IEF flux ratios in *ISO* spectra of the Carina nebula are independent of G_0 over $G_0 = 100 - 10^5$.

Much is yet to be gleaned from this *ISO* survey of reflection nebulae and especially the detection of IEFs toward vdB 133. In a future paper we will present a quantitative analysis of the IEF energy budget using laboratory absorption profiles of various carrier candidates (neutral PAHs, ionized PAHs, amorphous hydrocarbons, and coal tars). We will also present follow-up $7.75 \mu\text{m}$ (LW 6) *ISO* observations which cover an $8'$ by $8'$ mosaic around vdB 133, detailing the spatial distribution of the surrounding IEF emission. The relation of the IEF carriers to the gas and other components of dust surrounding vdB 133 will be explored by comparing the *ISO* images to ground-based infrared and molecular line (^{12}CO J=2-1) data that have also been obtained.

We would like to thank A. Léger, Jean-Loup Puget and C. Moutou for hosting us at the Institut d'Astrophysique Spatiale. We are grateful to W. Reach, D. Cesarsky and F. Boulanger for providing their expertise and invaluable help in the reduction of our ISOCAM data. We appreciate the generosity of D. Cesarsky and colleagues for providing us with their ISOCAM spectrum of NGC 7023, and F. Boulanger and colleagues for providing us with their ISOCAM spectrum of ρ Oph.

We acknowledge NASA support of the *ISO* data analysis through NAG 5-3366 and JPL contract 961562, and also support from NATO Collaborative Research Grant 951347. This work was carried out in part at the Jet Propulsion Laboratory, California Institute of Technology, under contract with the National Aeronautics and Space Administration.

REFERENCES

- Abergel, A., et al. 1996, *A&A*, 315, L329
- Aitken, D. K., 1981, in *IAU Symp. 96, Infrared Astronomy*, ed. C. G. Wynn-Williams & D. P. Cruikshank (Dordrecht: Reidel), 207
- Allamandola, L. J., Hudgins, D. M., & Sandford, S. A. 1999, *ApJ*, 511, L115
- Allamandola, L. J., Tielens, A. G. G. M., & Barker, J. R. 1985, *ApJ*, 290, L25
- Allamandola, L. J., Tielens, A. G. G. M., & Barker, J. R. 1989, *ApJS*, 71, 733
- Bakes, E. L. O., & Tielens, A. G. G. M. 1994, *ApJ*, 427, 822
- Bakes, E. L. O., & Tielens, A. G. G. M. 1998, *ApJ*, 499, 258
- Blanco, A., Bussoletti, E., & Colangeli, L. 1988, *ApJ*, 334, 875
- Borghesi, A., Bussoletti, E., & Colangeli, L. 1987, *ApJ*, 314, 422
- Boulanger, F., 1996, private communication
- Boulanger, F., Beichman, C., Désert, F.-X., Helou, G., Pérault, M., & Ryter, C. 1988, *ApJ*, 332, 328
- Boulanger, F., et al. 1996, *A&A*, 315, L325
- Boulanger, F., Boissel, P., Cesarsky, D., & Ryter, C. 1998a, *A&A*, 339, 194
- Boulanger, F., et al. 1998b, in *ASP Conf. Ser. 132, Star Formation with the Infrared Space Observatory*, ed. J. L. Yun & R. Liseau (San Francisco: ASP), 15
- Bregman, J. D., Allamandola, L. J., Witteborn, F. C., Tielens, A. G. G. M., Geballe, T. R. 1989, *ApJ*, 344, 791
- Bregman, J. D., Dinerstein, H. L., Goebel, J. H., Lester, D. F., Witteborn, F. C., & Rank, D. M. 1983, *ApJ*, 274, 666
- Brooke, T. Y., Sellgren, K., & Geballe, T. R. 1999, *ApJ*, 517, 883
- Brooke, T. Y., Sellgren, K., & Smith, R. G. 1996, *ApJ*, 459, 209
- Buss, R. H. Jr., Tielens, A. G. G. M., Cohen, M., Werner, M. W., Bregman, J. D., & Witteborn, F. C. 1993, *ApJ*, 415, 250
- Cesarsky, C. J., et al. 1996, *A&A*, 315, L32
- Cesarsky, D., Lequeux, J., Abergel, A., Pérault, M., Palazzi, E., Madden, S., Tran, D. 1996, *A&A*, 315, L309
- Chlewicki, G. & Laureijs, R. J. 1988, *A&A*, 207, L11

- Cohen, M., Allamandola, L. J., Tielens, A. G. G. M., Bregman, J. D., Simpson, J. P., Witteborn, F. C., Wooden, D. H., Rank, D. M. 1986, ApJ, 302, 737
- Cohen, M., Tielens, A. G. G. M., & Allamandola, L. J. 1985, ApJ, 299, L93
- Cohen, M., Tielens, A. G. G. M., Bregman, J. D., Witteborn, F. C., Rank, D. M., Allamandola, L. J., Wooden, D. H., Jourdain de Muizon, M. 1989, ApJ, 341, 246
- Cook, D. J., & Saykally, R. J. 1998, ApJ, 493, 793
- Crawford, M. K., Tielens, A. G. G. M., & Allamandola, L. J. 1985, ApJ, 293, L45
- Dartois, E., & d’Hendecourt, L. 1997, A&A, 323, 534
- De Frees, D. J., Miller, M. D., Talbi, D., Pauzat, F., & Ellinger, Y. 1993, ApJ, 408, 530
- de Geus, E. J., de Zeeuw, P. T., & Lub, J. 1989, A&A, 216, 44
- Désert, F.-X., Boulanger, F., & Puget, J. L. 1990, A&A, 237, 215
- Draine, B. T., & Anderson, N. 1985, ApJ, 292, 494
- Duley, W. W. 1988, MNRAS, 234, 61
- Duley, W. W., & Williams, D. A. 1981, MNRAS, 196, 269
- Duley, W. W., & Williams, D. A. 1988, MNRAS, 230, 1P
- Dwek, E., et al. 1997, ApJ, 475, 565
- Garmany, C. D., & Stencel, R. E. 1992, A&AS, 94, 211
- Geballe, T. R. 1997, in ASP Conf. Ser. 122, From Stardust to Planetesimals, ed. Y. J. Pendleton & A. G. G. M. Tielens (San Francisco: ASP), 119
- Geballe, T. R., Tielens, A. G. G. M., Kwok, S., & Hrivnak, B. J. 1992, ApJ, 387, L89
- Guillois, O., Nenner, I., Papoular, R., & Reynaud, C. 1996, ApJ, 464, 810
- Habing, H. J. 1968, Bull. Astron. Inst. Netherlands, 19, 421
- Helou, G., Ryter, C., & Soifer, B. T. 1991, ApJ, 376, 505
- Hudgins, D. M., Sandford, S. A., & Allamandola, L. J. 1994, J. Phys. Chem. 98, 4243
- Hudgins, D. M., & Allamandola, L. J. 1999a, ApJ, 513, L69
- Hudgins, D. M., & Allamandola, L. J. 1999b, ApJ, 516, L41
- Humphreys, R. M. 1978, ApJS, 38, 309
- ISOCAM Team 1994, in “ISOCAM Observer’s Manual”
- Joblin, C., Boissel, P., Léger, A., d’Hendecourt, D., & Défourneau, D. 1995, A&A, 299, 835
- Joblin, C., Léger, A., & Martin, P. 1992, ApJ, 393, L79

- Joblin, C., Tielens, A. G. G. M., Geballe, T. R., & Wooden, D. H. 1996, *ApJ*, 460, L119
- Jourdain de Muizon, M., d’Hendecourt, & Geballe, T. R. 1990, *A&A*, 227, 526
- Kessler, M. F., et al. 1996, *A&A*, 315, L27
- Kurucz, R. L. 1979, *ApJS*, 40, 1
- Kwok, S., Volk, K., & Hrivnak, B. J. 1989, *ApJ*, 345, L51
- Langhoff, S. R. 1996, *J. Phys. Chem.*, 100, 2819
- Laureijs, R. J., et al. 1996, *A&A*, 315, L317
- Le Coupanec, P., Rouan, D., & Léger, A. 1998, *A&A*, 338, 217
- Léger, A., & Puget, J. L. 1984, *A&A*, 137, L5
- Léger, A., Verstraete, L., d’Hendecourt, L., Défourneau, D., Dutuit, O., Schmidt, W., & Lauer, J. C. 1989, in *IAU Symp. 135, Interstellar Dust*, ed. L. J. Allamandola & A. G. G. M. Tielens (Dordrecht: Kluwer), 173
- Li, A., & Greenberg, J. M. 1997, *A&A*, 323, 566
- Lu, N. Y. 1998, *ApJ*, 498, L65
- Martini, P., Sellgren, K., & DePoy, D. L. 1999, *ApJ*, in press (astro-ph/9905028)
- Onaka, T. 1999, *Adv. Sp. Research*, in press
- Papoular, R., Conard, J., Guiliano, M., Kister, J., & Mille, G. 1989, *A&A*, 217, 204
- Papoular, R. 1999, *A&A*, 346, 219
- Pauzat, F., Talbi, D., & Ellinger, Y. 1995, *A&A*, 293, 263
- Pauzat, F., Talbi, D., & Ellinger, Y. 1997, *A&A*, 319, 318
- Platt, J. R. 1956, *ApJ*, 123, 486
- Puget, J. L., Léger, A. 1989, *ARA&A*, 27, 161
- Puget, J. L., Léger, A. & Boulanger, F. 1985, *A&A*, 142, L19
- Racine, R. 1968 *AJ*, 73, 233
- Roche, P. F., & Aitken, D. K. 1986, *MNRAS*, 221, 63
- Rowan-Robinson, M. 1992, *MNRAS*, 258, 787
- Ryter, C., Puget, J. L., & Péroult, M. 1987, *A&A*, 186, 312
- Sakata, A., Wada, S., Onaka, T., & Tokunaga, A. 1987, *ApJ*, 320, L63
- Sakata, A., Wada, S., Tanabe, T., & Onaka, T. 1984, *ApJ*, 287, L51
- Salama, F., Bakes, E. L. O., Allamandola, L. J., & Tielens, A. G. G. M. 1996, *ApJ*, 458, 621

- Schutte, W. A., Tielens, A. G. G. M., & Allamandola, L. J. 1993, *ApJ*, 415, 397
- Schutte, W. A., et al. 1996, *A&A*, 315, L333
- Schutte, W. A., et al. 1998, *A&A*, 337, 261
- Sellgren, K. 1984, *ApJ*, 277, 623
- Sellgren, K. 1990, in *Dusty Objects in the Universe*, ed. E. Bussoletti & A. A. Vittone (Dordrecht: Kluwer), 35
- Sellgren, K. 1994, in *The Infrared Cirrus and Diffuse Interstellar Clouds*, ed. R. M. Cutri & W. B. Latter (San Francisco: ASP), 243
- Sellgren, K., Brooke, T. Y., Smith, R. G., & Geballe, T. R. 1995, *ApJ*, 449, L69
- Sellgren, K., Luan, L., & Werner, M. W. 1990, *ApJ*, 359, 384
- Sellgren, K., Smith, R. G., & Brooke, T. Y. 1994, *ApJ*, 433, 179
- Sellgren, K., Werner, M. W., & Allamandola, L. J. 1996, *ApJS*, 102, 369
- Sellgren, K., Werner, M. W., & Dinerstein, H. L. 1983, *ApJ*, 271, L13
- Sellgren, K., et al. 1999, in preparation
- Siebenmorgen, R., & Krügel, E. 1992, *A&A*, 259, 614
- Silva, L., Granato, G. L., Bressan, A., & Danese, L. 1998, *ApJ*, 509, 103
- Spaans, M., Tielens, A. G. G. M., van Dishoeck, E. F., & Bakes, E. L. O. 1994, *ApJ*, 437, 270
- Strom, S. E., Grasdalen, G. L., & Strom, K. M. 1974, *ApJ*, 191, 111
- Strom, K. M., Strom, S. E., Carrasco, L., Vrba, F. J. 1975, *ApJ*, 196, 489
- Szczepanski, J. & Vala, M. 1993, *ApJ*, 414, 646
- Tokunaga, A. 1997, in *ASP Conf. Ser. 124, Diffuse Infrared Radiation and the IRTS*, ed. H. Okuda, T. Matsumoto, & T. L. Roellig (San Francisco: ASP), 149
- Uchida, K. I., Sellgren, K., & Werner, M. 1998, *ApJ*, 493, L109 (Paper I)
- Whitcomb, S. E., Gatley, I., Hildebrand, R. H., Keene, J., Sellgren, K. & Werner, M. W. 1981, *ApJ*, 246, 416
- Witt, A. N., Cottrell, M. J. 1980, *ApJ*, 235, 899
- Wolfire, M. G., Hollenbach, D., McKee, C. F., Tielens, A. G. G. M., & Bakes, E. L. O. 1995, *ApJ*, 443, 152
- Zavagno, A., Cox, P., & Baluteau, J.-P. 1992, *A&A*, 259, 241

Table 1. Stellar Data

Nebula ^a	Star	Spectral Type	T_{eff}	$\frac{F_{(\lambda < 400\text{nm})}}{F_{\text{total}}}$	$\frac{F_{(\lambda < 240\text{nm})}}{F_{\text{total}}}$	$\frac{\Delta\nu I_{\nu}(12\mu\text{m})^b}{I_{\text{bol}}(FIR)}$	Refs ^g
Observed Sources^c							
vdB 17	BD +30 549	B8 V	11,000	0.55	0.33	0.09	1
vdB 59	HD 38563B	B2 II–III	19,000	0.87	0.69	0.14	2
vdB 101	HD 146834	G5 III	5,000	0.07	0.003	0.29	1
vdB 111	HD 156697	F0 n	7,300	0.15 – 0.20 ^d	0.02 – 0.03	0.21	1
vdB 133	HD 195593(A + B)	F5 Iab + B7 II	6,800 + 12,000	0.22 ^e	0.09 ^e	0.19	1,3
vdB 135	BD +31 4152	M1 IIIe	3,600	0.01	0.00005	0.11	1
Comparison Sources							
vdB 139	HD 200775	B3 IVe	17,000	0.84	0.65	0.09	1,4
vdB 106	HD 147933 + HD 147934	B2 IV-V + B2 IV-V	22,000 + 22,000	0.92 ^e	0.77 ^f	...	5

^avdB 17 = NGC 1333, vdB 59 = NGC 2068, vdB 106 = ρ Oph, and vdB 139 = NGC 7023.

^bBased on data from Tables 2 and 3 in Sellgren et al. 1990. The adopted width of the 12 μm IRAS bandpass is 1.75×10^{13} Hz.

^cSources observed in this study

^dThe range in $F_{(\lambda < 400\text{nm})}/F_{\text{total}}$ and $F_{(\lambda < 240\text{nm})}/F_{\text{total}}$ stems from the uncertainty in the luminosity class of vdB 111.

^e $F_{(\lambda < 400\text{nm})}/F_{\text{total}}$ for vdB 133 is equal to the sum of $F_{(\lambda < 400\text{nm})}$ for stars A and B divided by the sum of F_{total} for stars A and B. $F_{(\lambda < 240\text{nm})}/F_{\text{total}}$ for vdB 133 is equal to the sum of $F_{(\lambda < 240\text{nm})}$ for stars A and B divided by the sum of F_{total} for stars A and B.

^f $F_{(\lambda < 400\text{nm})}/F_{\text{total}}$ for ρ Oph is equal to the sum of $F_{(\lambda < 400\text{nm})}$ for stars HD 147933 and HD 147934 divided by the sum of F_{total} for stars HD 147933 and HD 147934. $F_{(\lambda < 240\text{nm})}/F_{\text{total}}$ for ρ Oph is equal to the sum of $F_{(\lambda < 240\text{nm})}$ for stars HD 147933 and HD 147934 divided by the sum of F_{total} for stars HD 147933 and HD 147934.

^gSpectral classification references: (1) Racine 1968; (2) Strom et al. 1975; (3) Uchida, Sellgren, & Werner 1998 (Paper I); (4) Witt & Cottrell 1980; (5) de Geus, de Zeeuw, & Lub 1989.

Table 2. Observation Sequences

Sequence	Wavelengths (μm) ^a	Observed Sources (vdB)
1a	5.8, 6.2, 7.0, 9.5	101, 133, 135
1b	4.5 ^b , 6.2, 7.0, 9.5	111
2	7.0, 7.6, 8.4	101, 111, 133, 135
3	8.4, 8.62, 9.5	101, 111, 133
4	10.5, 11.22, 12.0, 15.0 ^c	101, 111, 133, 135

^aUnless otherwise noted all wavelengths refer to circular variable filter settings, which have a spectral resolution $\lambda/\Delta\lambda = 40$.

^bNarrowband filter LW1 ($\Delta\lambda = 1 \mu\text{m}$).

^cNarrowband filter LW9 ($\Delta\lambda = 2 \mu\text{m}$).

Table 3. Field Positions

Nebula	Stellar Position		Source offset from star		Sky offset from star	
	RA (2000)	Dec (2000)	$\Delta\text{RA} (")$	$\Delta\text{Dec} (")$	$\Delta\text{RA} (")$	$\Delta\text{Dec} (")$
Position Switched Observations						
vdB 101	16 19 07.5	−20 13 03.9	0	0	+562	−112
vdB 111	17 18 52.7	06 05 07.1	0	0	+498	+160
vdB 133	20 30 59.1	36 56 09.2	0	0	−1187	+266
vdB 135	20 36 45.5	32 27 17.3	0	0	−1218	−97
Full CVF Scan Observations						
vdB 17 (NGC 1333)	03 29 19.8	31 24 56.0	+12	−26	+493	+12
vdB 59 (NGC 2068)	05 46 44.6	00 05 22.6	+92	+12	+1026	+13
vdB 101	16 19 07.5	−20 13 03.9	+39	+20	+470	−24
vdB 133	20 30 59.1	36 56 09.2	+134	+67	+704	+102
vdB 135	20 36 45.5	32 27 17.3	−96	+201	−771	−86

Table 4. The Integration Regions

Nebula	Region Center ^a		Region Size		PA ^b (°)	Comments ^c
	$\Delta\text{RA}(\prime\prime)$	$\Delta\text{Dec}(\prime\prime)$	$\Delta X(\prime\prime)$	$\Delta Y(\prime\prime)$		
<hr/>						
Position Switched Observations						
vdB 101	0	0	150	150	9.4	ER, XS
vdB 111	0	0	150	150	85.9	ER, XS
vdB 133	+72	+46	66	30	20.7	LE, XS
vdB 135	0	0	150	150	5.6	ER, XS
<hr/>						
Full CVF Scan Observations						
vdB 17 (NGC 1333)	+14	-22	60	60	77.7	LE
vdB 59 (NGC 2068)	+90	+28	72	78	5.8	LE
vdB 101	+34	+227	192	192	10.1	ER
vdB 133	+85	+43	60	48	83.8	LE
vdB 135	-104	+204	192	192	65.5	ER

^a offset of the integration region center from the central star.

^b The rotation of the Y-axis east of celestial north.

^c Describes the subregion used to produce the spectral averages: LE — containing localized IEF emission, ER — the entire usable portion of the image, XS — excluding the emission from the central star.

Note. — Columns 2 and 3 give the location of the subregion center in ΔRA , ΔDec offsets from the illuminating star(s), columns 4 and 5 its ΔX and ΔY dimensions, respectively, and column 6 the position angle of its Y-axis with respect to celestial north. Column 7 provides the brief description of the region, whether it encompasses the entire usable area of the array (ER — entire region), or a localized patch of IEF emission (LE — localized emission). In those cases where the image contained the illuminating star (the position switched data), the star and the immediate region containing a spurious arc-like reflection feature from the star (typically pixels $X, Y = [6-20, 11-24]$ of the array) were excluded (XS; excluded star) from the spatial integration.

Table 5. Nebular Illumination

Nebula	Nebula distance (pc)	θ_{Neb}^a (arcsec)	G_0 (91 nm < λ < 240 nm) ^b	Refs ^c
<hr/>				
Observed Sources				
vdB 17 (NGC 1333)	500	29	175	1
vdB 59 (NGC 2068)	550	93	520	2
vdB 133	1500	100	75	3, 4
<hr/>				
Observed Sources				
vdB 139 (NGC 7023)	440	43	1820	5
vdB 106 (ρ Oph)	125	2400	40	6

^aThe angular distance between illuminating star and the observed nebular region.

^b G_0 , the UV (91 nm < λ < 240 nm) radiation field at the nebula, due to the illuminating stars, in units of 1.6×10^{-3} ergs s⁻¹ cm⁻², the local interstellar radiation field as determined by Habing 1968

^c Distance references: (1) Strom, Grasdalen, & Strom 1974; (2) Racine 1968; (3) Humphreys 1978; (4) Garmany & Stencel 1992; (5) Whitcomb et al. 1981; (6) de Geus, de Zeeuw, & Lub 1989.

Table 6. Normalized Integrated Line Fluxes

		Observed Sources			Comparison Sources	
		vdB 17 ^a	vdB 59	vdB 133	vdB 139	vdB 106
Method 1 Fluxes ^b						
IEFs	(6.2 μm)/(11.3 μm)	1.4	1.7	1.0	1.1	1.2
	(7.7 μm)/(11.3 μm)	3.8	4.4	4.8	3.4	4.1
	(8.6 μm)/(11.3 μm)	2.0	2.3	2.9	1.8	2.0
	(12.7 μm)/(11.3 μm)	0.18	0.30	0.29	0.21	0.21
Broad Bumps	(6 – 9 μm)/(11.3 μm)	3.0	2.7	2.6	2.5	2.7
	(11 – 13 μm)/(11.3 μm)	1.6	1.2	1.1	1.4	1.8
Continuum	(5.2 – 15.1 μm)/(11.3 μm)	6.1	4.6	7.1	5.0	6.5
Method 2 Fluxes						
IEFs	(6.2 μm)/(11.3 μm)	1.2	1.7	1.3	1.2	1.4
	(7.7 μm)/(11.3 μm)	1.7	2.0	2.3	2.0	2.0
	(8.6 μm)/(11.3 μm)	0.28	0.44	0.29	0.24	0.36
	(12.7 μm)/(11.3 μm)	0.18	0.18	0.24	0.30	0.23
Continuum	(5.2 – 15.1 μm)/(11.3 μm)	14.0	11.0	15.0	13.0	15.0
Method 3 Fluxes						
IEFs	(6.2 μm)/(11.3 μm)	1.4	1.8	1.0	1.2	1.0
	(7.7 μm)/(11.3 μm)	2.3	3.0	2.4	2.5	2.1
	(8.6 μm)/(11.3 μm)	1.4	1.7	1.7	1.3	1.3
	(12.7 μm)/(11.3 μm)	0.87	0.50	0.50	0.63	0.60
Continuum	(5 – 15 μm)/(11.3 μm)	3.6	3.7	2.3	3.1	2.6
11.3 μm Line Fluxes ^c						
Method 1 (11.3 μm)		1.3e–3	2.8e–3	1.5e–4	... ^d	3.3e–4
Method 2 (11.3 μm)		1.3e–3	3.2e–3	1.5e–4	... ^d	3.3e–4
Method 3 (11.3 μm)		2.2e–3	4.0e–3	3.2e–4	... ^d	6.9e–4
Total Band Fluxes						
IRAS 12 μm ^e		1.1e–2	2.0e–2	1.4e–3	... ^g	3.0e–3
ISO LW 2 ^f		7.6e–4	1.7e–3	9.6e–5	... ^g	1.9e–4

^avdB 17 = NGC 1333, vdB 59 = NGC 2068, vdB 139 = NGC 7023, and vdB 106 = ρ Oph.

^bIntegrated line flux from listed spectral feature (ergs s⁻¹ cm⁻² sr⁻¹) divided by the integrated flux within the 11.3 μm feature.

^cTotal integrated 11.3 μm line flux in units of ergs s⁻¹ cm⁻² sr⁻¹.

^dNo integrated 11.3 μm line flux of vdB 139 is presented since only a scaled version of the spectrum was available to us.

^eTotal integrated source flux (ergs s⁻¹ cm⁻² sr⁻¹) expected in 12 μm IRAS band, found by the convolution of the source CVF spectrum with the 12 μm IRAS bandpass.

^fTotal integrated source flux (ergs s⁻¹ cm⁻² sr⁻¹) expected in ISO LW 2 band, found by the convolution of the source CVF spectrum with the ISO LW 2 bandpass.

^gNo integrated 12 μm line flux of vdB 139 is presented since only a scaled version of the spectrum was available to us.

Table 7. Normalized Bandpass Fluxes

	Filter	
	IRAS 12 μm	ISO LW 2
<hr/> <hr/>		
Method 1 Fluxes		
IEFs/(Total ^a)	0.35 – 0.51 ^b	0.52 – 0.59
Broad Bumps/Total	0.10 – 0.18	0.22 – 0.26
Continuum/Total	0.33 – 0.45	0.18 – 0.22
<hr/>		
Method 2 Fluxes		
IEFs/Total	0.18 – 0.26	0.26 – 0.35
Continuum/Total	0.74 – 0.82	0.65 – 0.73
<hr/>		
Method 3 Fluxes		
IEFs/Total	0.58 – 0.67	0.64 – 0.71
Continuum/Total	0.29 – 0.47	0.15 – 0.22

^aIntegrated flux of the spectral feature ($\text{erg cm}^{-2} \text{s}^{-1} \text{sr}^{-1}$) divided by the integrated flux within the broadband filter (IRAS 12 μm or ISO LW 2) found by the convolution of the source CVF spectrum with the bandpass function.

^bThe range of values presented represent the minimum and maximum from among the five sources, vdB 17 (NGC 1333), vdB 59 (NGC 2068), vdB 133, vdB 139 (NGC 7023), vdB 106 (ρ Oph).

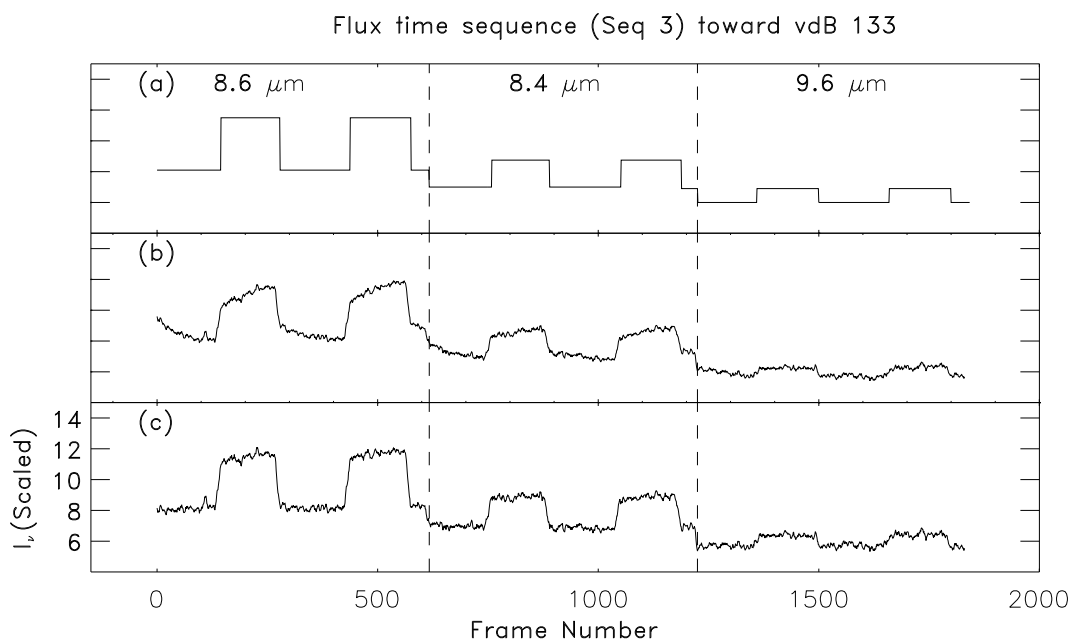


Fig. 1.— Rectification of ISOCAM data for Sequence 3 for vdB 133, during a 2 cycle sky \rightarrow source observational sequence done consecutively with three different circular variable filter (CVF) settings at wavelengths of 8.6, 8.4, and 9.6 μm . The horizontal axis is image frame number; each image was obtained with an integration time of 0.28 s. *a*: the ideal response of the detector. *b*: an actual observation sequence toward vdB 133 showing the deviation from the ideal due to the detector flux transient response. *c*: the data of panel *b* after application of the flux “rectification” procedure.

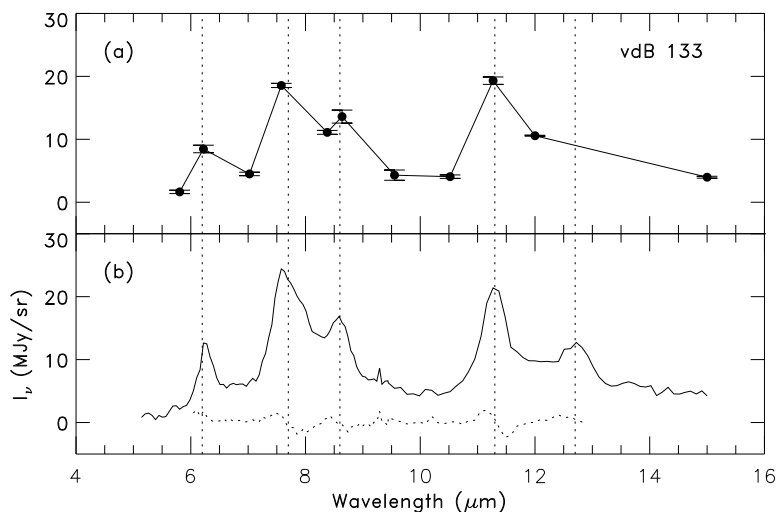


Fig. 2.— Flux-rectified and sky-subtracted 5.1 – 15 μm spectra of vdB 133, in I_ν (MJy sr^{-1}) vs. $\lambda(\mu\text{m})$. Wavelengths of the 6.2, 7.7, 8.6, 11.3, and 12.7 μm infrared emission features (IEFs) are marked (*dotted vertical lines*). (a) Spectrum from position-switched observations at chosen CVF wavelengths (*filled circles*). Error bars show the difference between the cycle 1 and cycle 2 source–sky rectified data at each wavelength. (b) Spectrum from complete CVF scan (*solid line*). The difference between the rectified increasing and decreasing wavelength scans of the source-sky spectra (*dotted line*) is plotted as an estimate of the uncertainty.

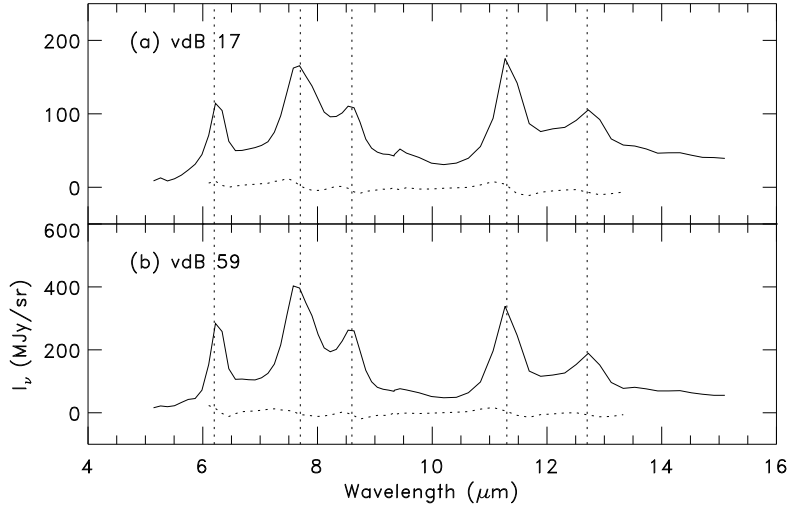


Fig. 3.— Flux-rectified, sky-subtracted 5.1 – 15 μm spectra (*solid line*) from complete CVF scans of (a) vdB 17 (NGC 1333), and (b) vdB 59 (NGC 2068), in I_ν (MJy sr^{-1}) vs. $\lambda(\mu\text{m})$. The wavelengths of the 6.2, 7.7, 8.6, 11.3, and 12.7 μm IEFs are marked (*dotted vertical lines*). The difference between the rectified increasing and decreasing wavelength scans of the source-sky spectra (*dotted line*) is plotted as an estimate of the uncertainty.

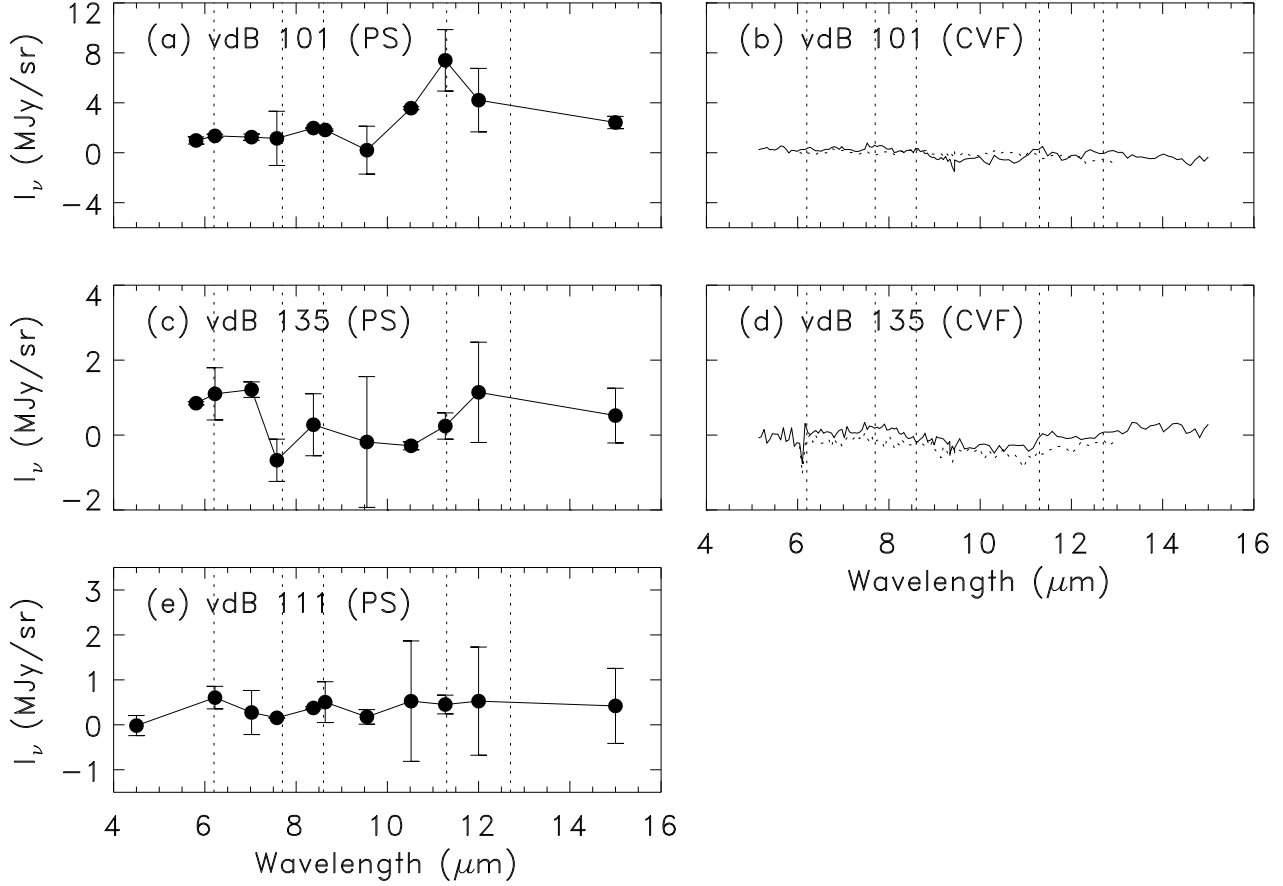


Fig. 4.— Flux-rectified and sky-subtracted 5.1 – 15 μm spectra of (a, b) vdB 101, (c, d) vdB 135, and (e) vdB 111, in I_ν (MJy sr $^{-1}$) vs. λ (μm). Wavelengths of the 6.2, 7.7, 8.6, 11.3, and 12.7 μm IEFs are marked (*dotted vertical lines*). (a, c, e) Spectra from position-switched observations at chosen CVF wavelengths (*filled circles*). Error bars show the difference between the cycle 1 and cycle 2 source–sky rectified data at each wavelength. (b, d) Spectra from complete CVF scan (*solid line*). The difference between the rectified increasing and decreasing wavelength scans of the source-sky spectra (*dotted line*) is plotted as an estimate of the uncertainty.

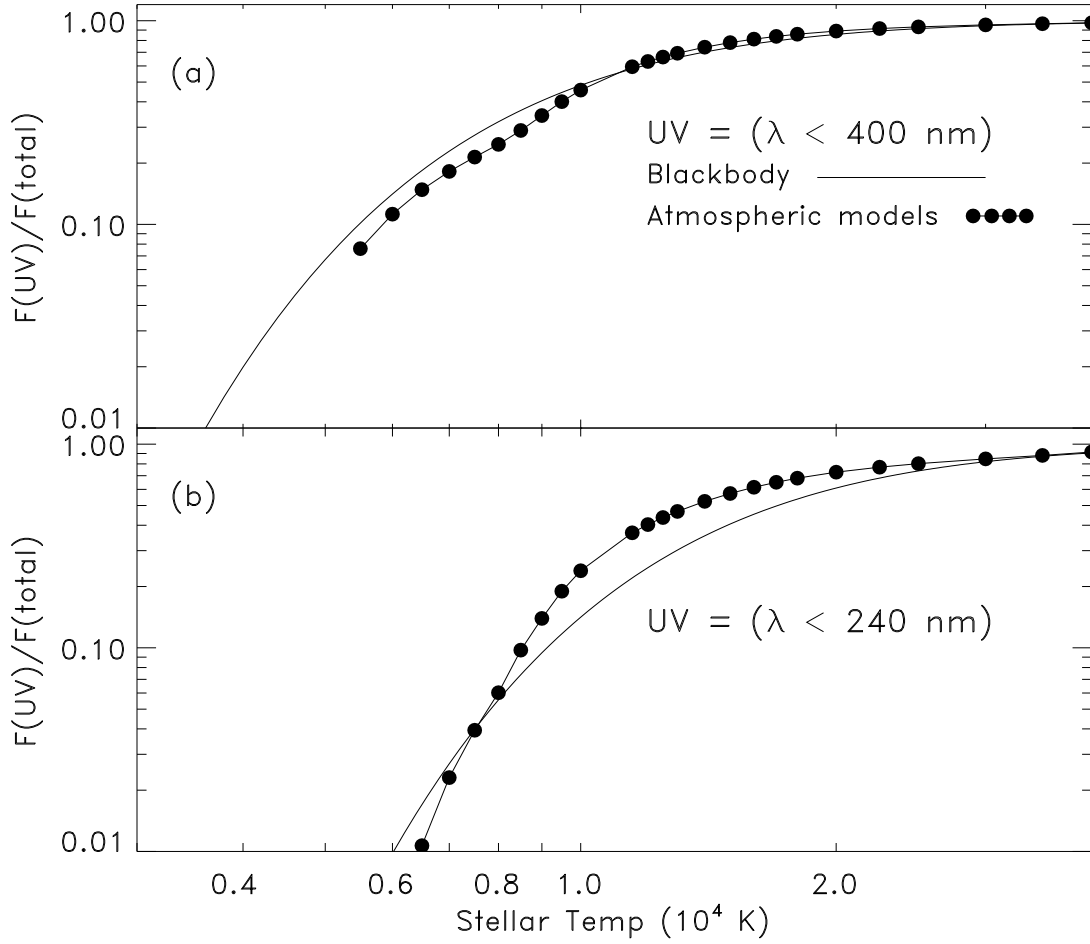


Fig. 5.— Plots of the fraction of UV emission to total emission as a function of stellar temperature, calculated from (*connected dots*) Kurucz (1979) atmospheric models with $\log(g) = 4.0$ and from (*solid line*) a blackbody. The UV range is defined as (a) $\lambda < 400$ nm or (b) $\lambda < 240$ nm.

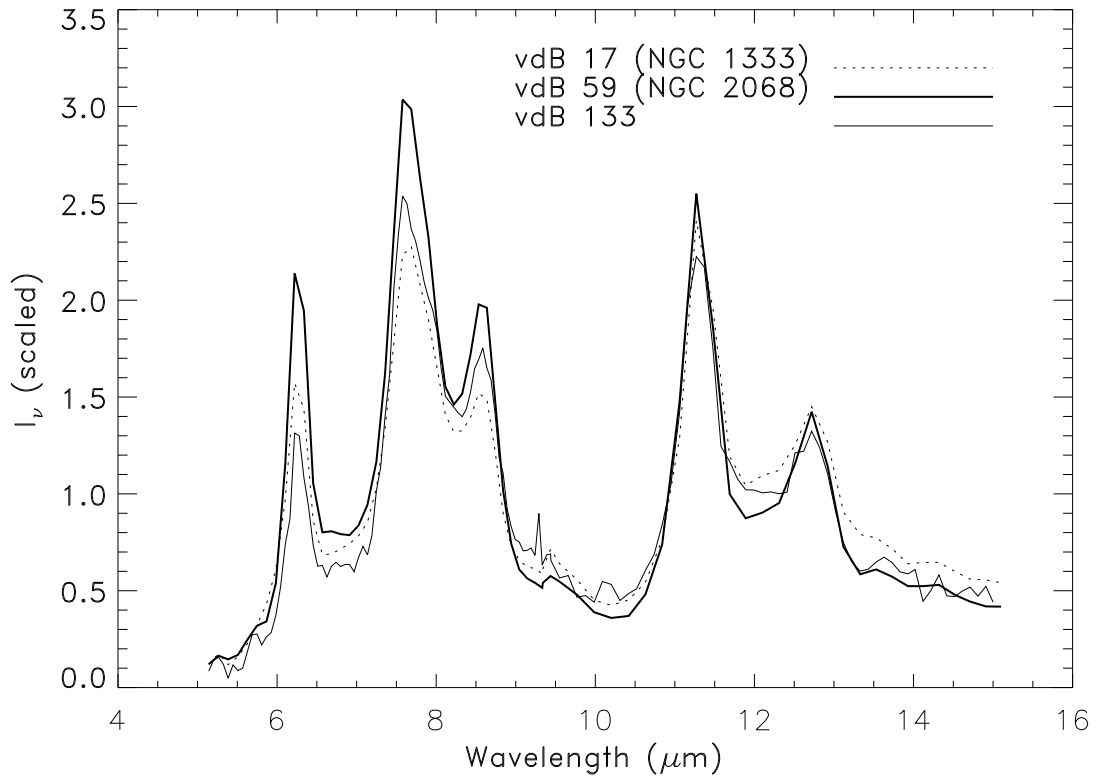


Fig. 6.— Superposed spectra of (*dotted line*) vdB17 (NGC 1333), (*thick solid line*) vdB59 (NGC 2068), and (*thin solid line*) vdB133. Spectra are I_ν (MJy sr⁻¹), divided by their intensity in the *IRAS* 12 μ m broad-band filter (MJy sr⁻¹), vs. $\lambda(\mu\text{m})$. The fraction of total stellar flux emitted at UV wavelengths, for the illuminating stars of these reflection nebulae, is lowest for vdB133 and highest for vdB59.

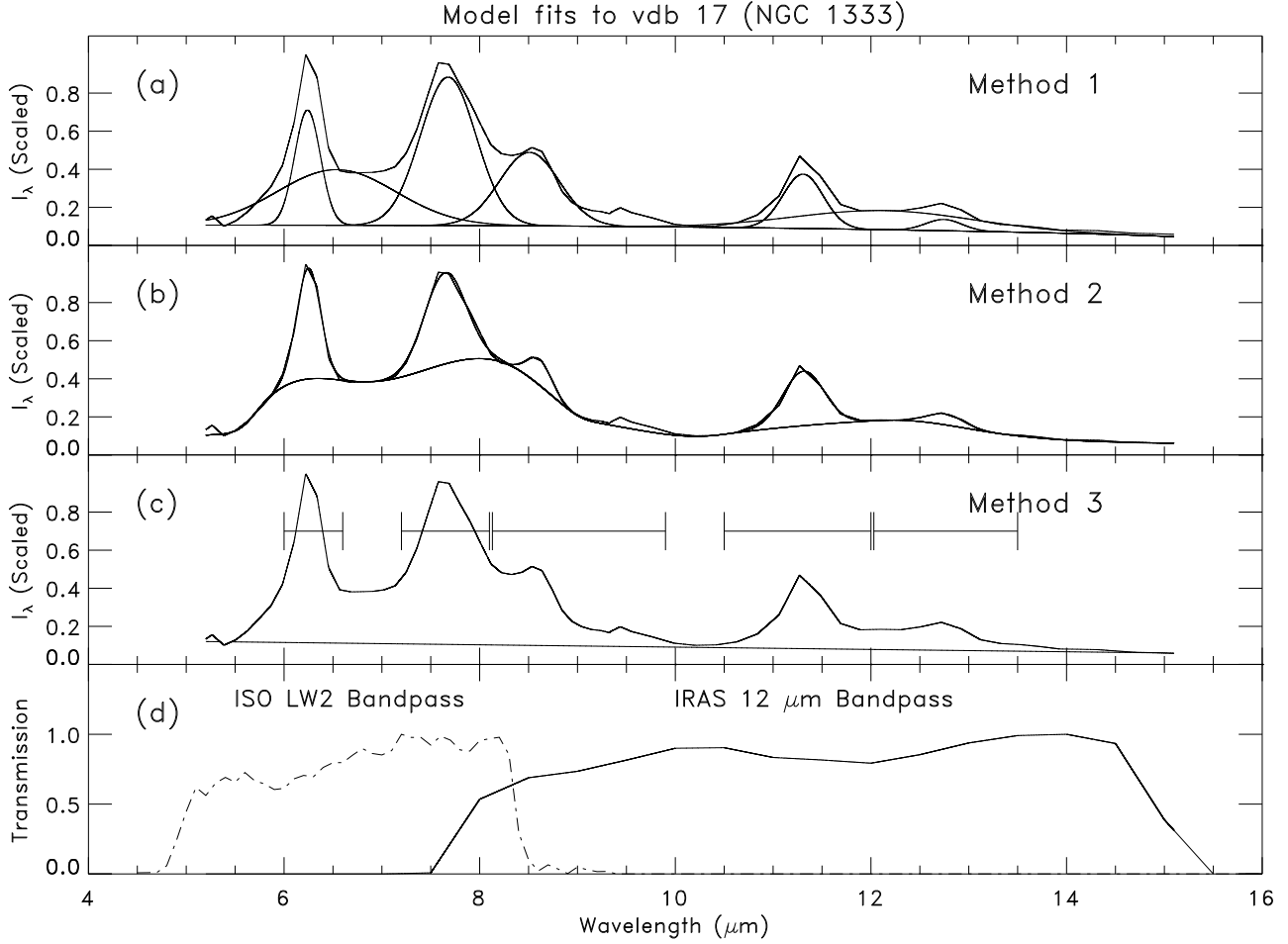


Fig. 7.— The 5 – 15 μm spectrum of vdB17 (NGC1333) superposed with feature and continuum components fitted by (a) Method 1, (b) Method 2, and (c) Method 3 (see text). The integration regions adopted for the various IEFs in Method 3 (c) are marked (*horizontal bars*). The ISO LW 2 and IRAS 12 μm filter transmission functions are also plotted (d). Note spectra are plotted as $I_\lambda(\text{erg cm}^{-2} \text{s}^{-1} \text{sr}^{-1})$ vs. $\lambda(\mu\text{m})$, which differs from other figures.

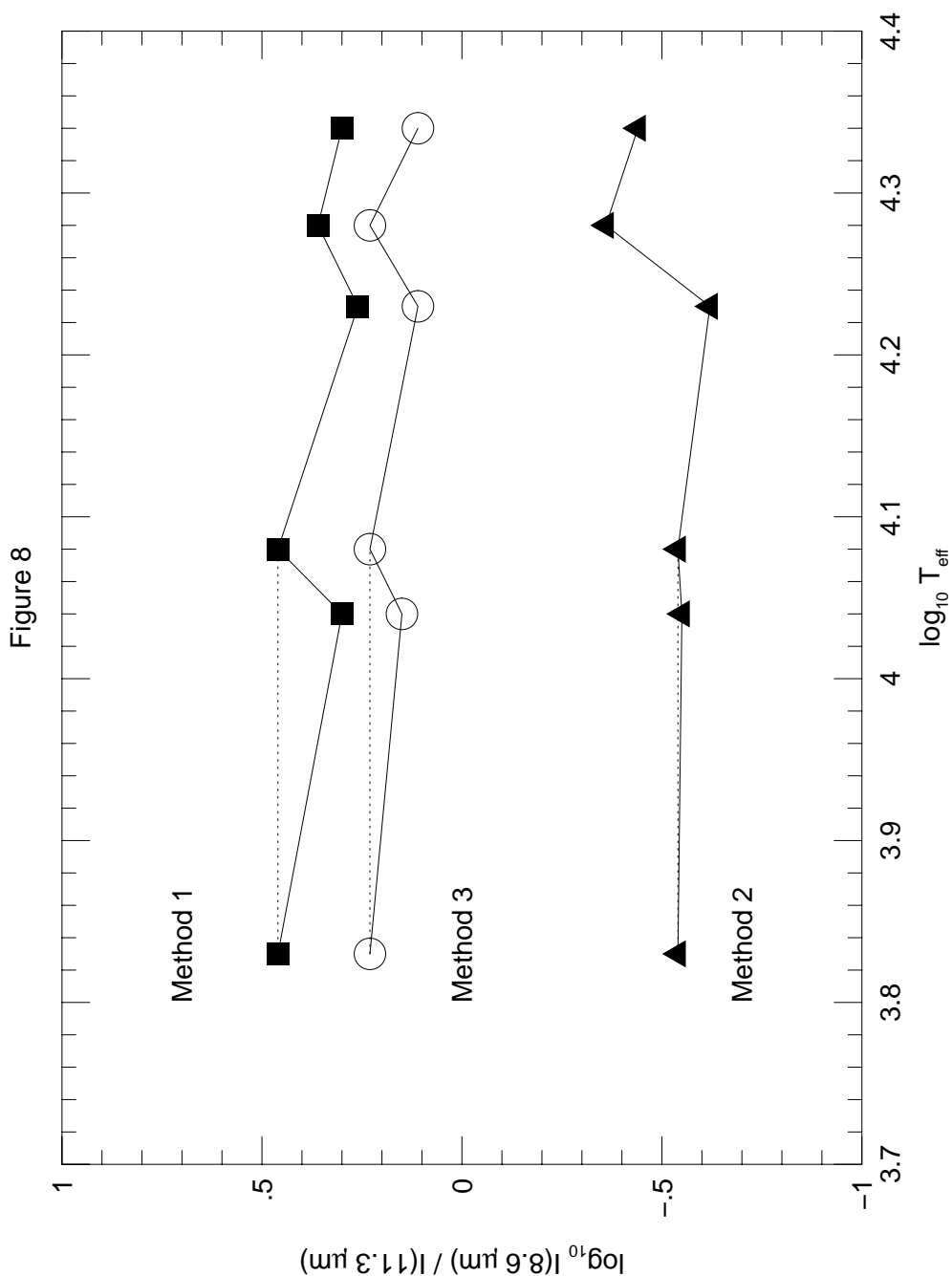


Fig. 8.— Plot displaying $\log[F(8.6 \mu\text{m})/F(11.3 \mu\text{m})]$, the ratio of integrated $8.6 \mu\text{m}$ and $11.3 \mu\text{m}$ IEF fluxes ($\text{erg cm}^{-2} \text{s}^{-1} \text{sr}^{-1}$), vs. $\log(T_{\text{eff}})$, the effective temperature of the illuminating star(s) of each reflection nebula. Values of $\log[F(8.6 \mu\text{m})/F(11.3 \mu\text{m})]$ determined by Method 1 (*filled squares*), Method 2 (*filled triangles*), and Method 3 (*open circles*) are compared (see text). Values of $\log[F(8.6 \mu\text{m})/F(11.3 \mu\text{m})]$ for each Method are connected (*solid lines*) for clarity. Values of $\log[F(8.6 \mu\text{m})/F(11.3 \mu\text{m})]$ are plotted at two values of T_{eff} , corresponding to the hotter and cooler illuminating star of vdB 133 (points connected by *dotted lines*).

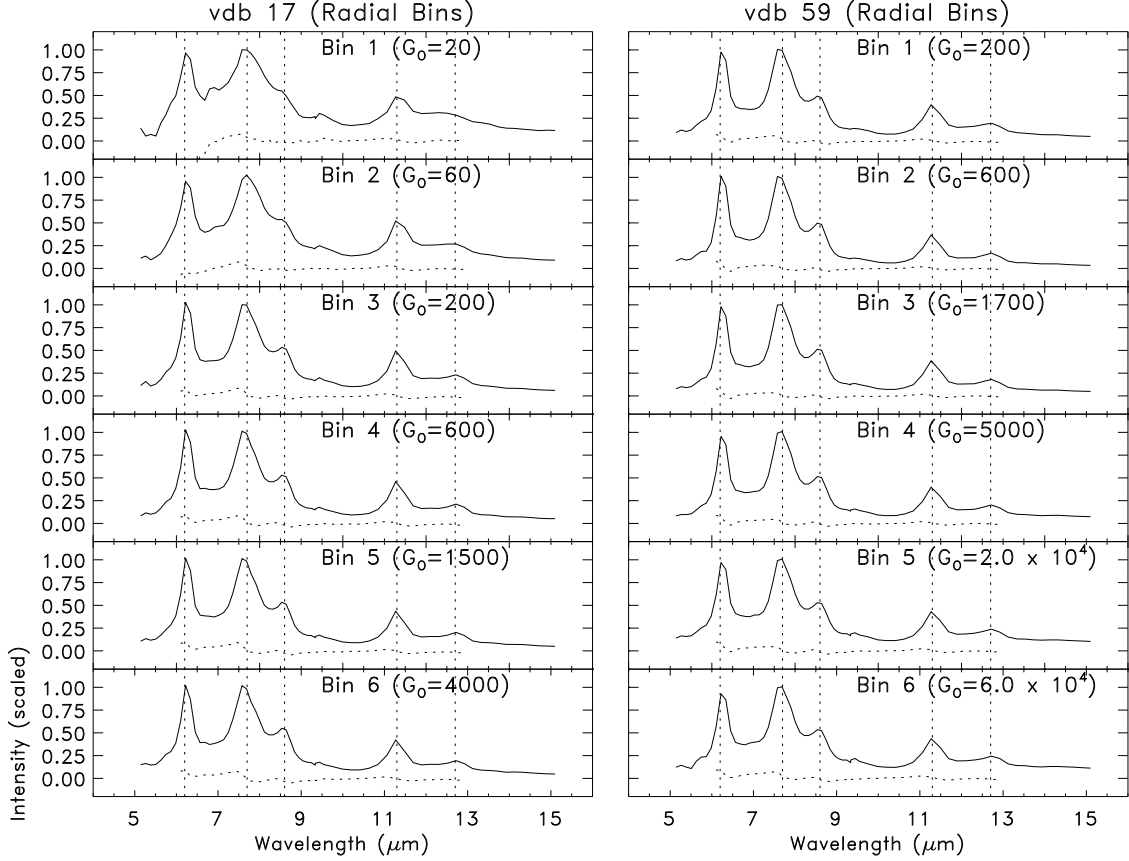


Fig. 9.— Spectra (*solid lines*) of vdB 17 (*left*) and vdB 59 (*right*), averaged over radial bins of projected distance from the illuminating star. Radial bins are characterized by the UV field, G_0 , incident on each nebular annulus (see text). G_0 is in units of 1.6×10^{-3} ergs $s^{-1} \text{ cm}^{-2}$, the local interstellar radiation field as determined by Habing (1968). Bins with values of $G_0 = 20, 60, 200, 600, 1500,$ and 4000 (*top to bottom*) are shown for vdB 17. Bins with values of $G_0 = 200, 600, 1700, 5000, 2.0 \times 10^4,$ and 6.0×10^4 (*top to bottom*) are shown for vdB 59. Spectra are I_ν (MJy sr^{-1}), divided by the peak value of I_ν at 7, 8.6, 11.3, and $12.7 \mu\text{m}$. IEFs are marked (*dotted vertical lines*). The difference between the rectified increasing and decreasing wavelength scans of the source-sky spectra (*dotted line*) is plotted as an estimate of the uncertainty.

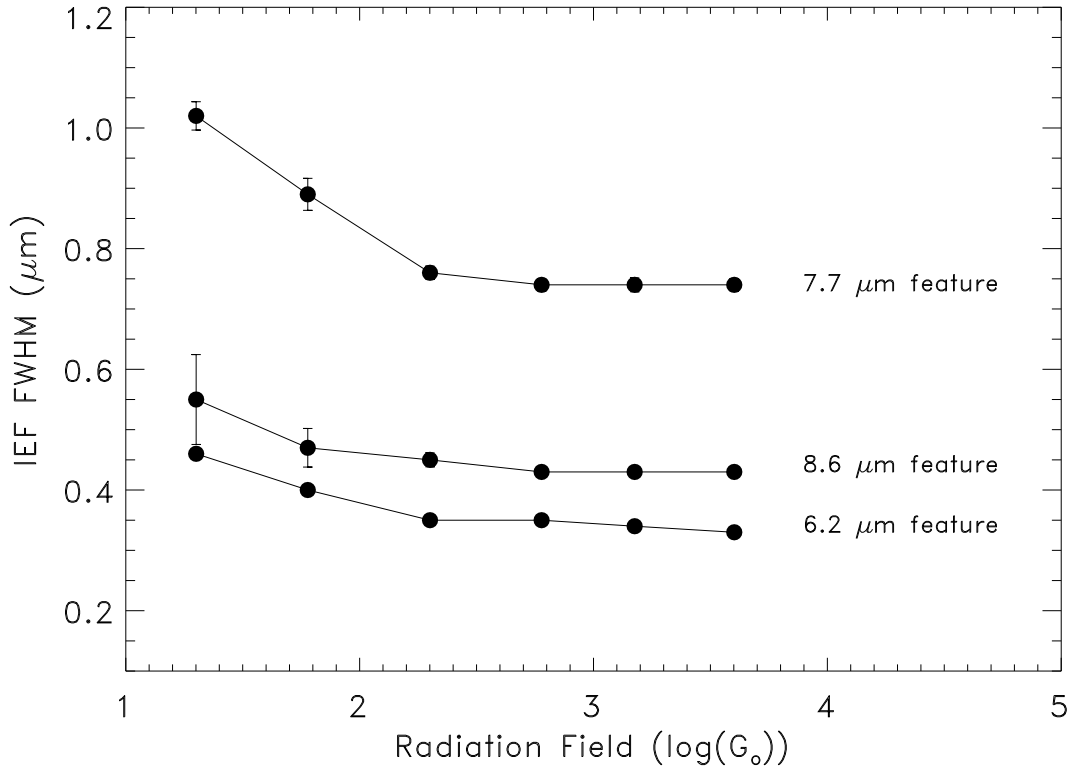


Fig. 10.— Full-width at half-maximum (FWHM) of the 6.2 μm , 7.7 μm , and 8.6 μm IEFs vs. incident UV intensity, $\log(G_0)$, for different nebular positions within vdB 17. FWHM were derived by Lorentzian fits to the spectra shown in Fig. 9 (see text). Error bars for each radial bin or annulus are derived from the difference between spectra of the top half of the annulus and the bottom half of the annulus.

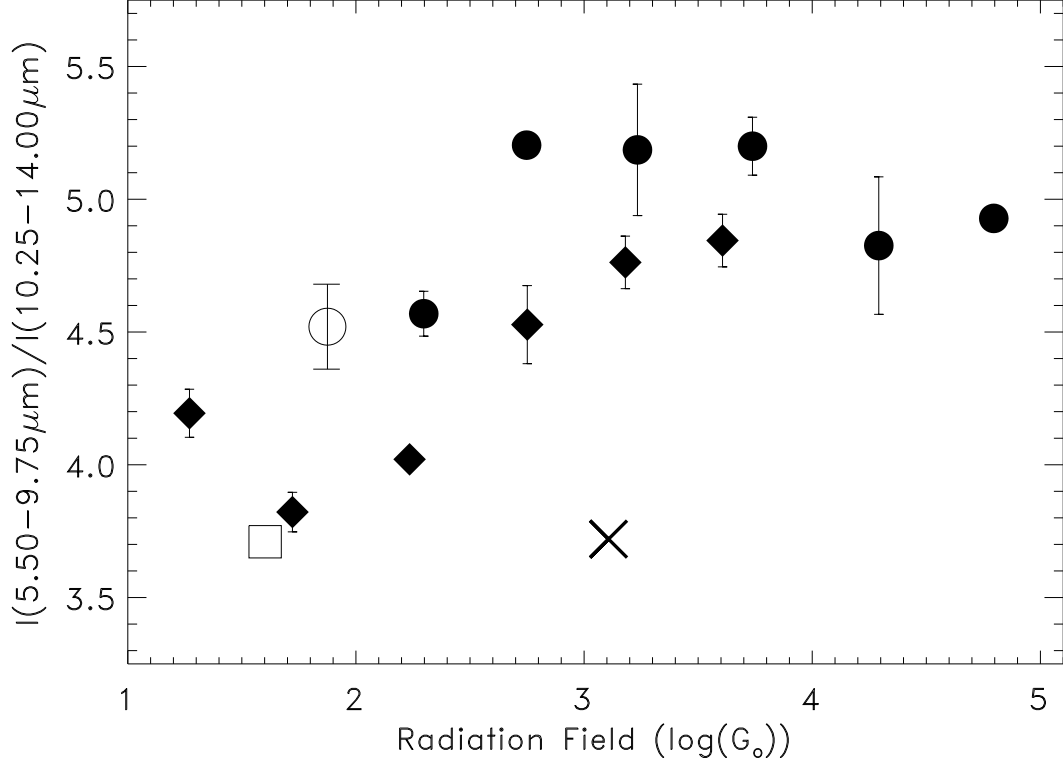


Fig. 11.— Ratio of the integrated spectral intensity at $5.50 - 9.75 \mu\text{m}$ to the integrated spectral intensity at $10.25 - 14.0 \mu\text{m}$, $I(5.50-9.75 \mu\text{m})/I(10.25-14.0 \mu\text{m})$, vs. the incident UV intensity, $\log(G_0)$. Ratios at different nebular positions within vdB 17 (NGC 1333; *filled diamonds*) and vdB 59 (NGC 2068; *filled circles*) are derived from spectra in Fig. 9. Ratios for the spatially averaged spectra of vdB 133 (*open circle*; Fig. 2*b* and Paper I), vdB 106 = ρ Oph (*open square*; Boulanger et al. 1996), and vdB 139 = NGC 7023 (*cross*; D. Cesarsky et al. 1996) are also plotted. Error bars for vdB 133 are derived from the difference between the rectified increasing and decreasing wavelength scans of the source-sky spectra. Error bars for each radial bin or annulus in vdB 17 are derived from the difference between spectra of the top half of the annulus and the bottom half of the annulus. Error bars for each radial bin or annulus in vdB 59 are derived from the difference between spectra of the right half of the annulus and the left half of the annulus.